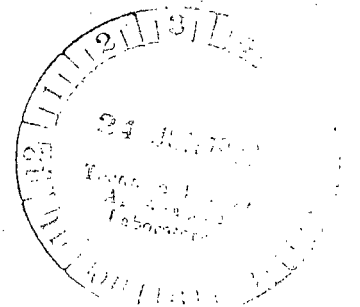NASA
TP
2010
c.1

Comparison of Analytical and Wind-Tunnel Results for Flutter and Gust Response of a Transport Wing With Active Controls

Irving Abel,
Boyd Perry III,
and Jerry R. Newsom

NASA

Comparison of Analytical and Wind-Tunnel Results for Flutter and Gust Response of a Transport Wing With Active Controls

Irving Abel,
Boyd Perry III,
and Jerry R. Newsom
*Langley Research Center
Hampton, Virginia*

INTRODUCTION

The application of active controls technology to both derivative and new commercial transport designs offers the potential for substantial improvements in aircraft energy efficiency. This improvement can be a direct result of using active controls to provide such functions as relaxed static stability or load alleviation. Active controls can also be used indirectly by allowing advanced aerodynamic features such as winglets and supercritical airfoils to be used without paying a penalty in terms of flutter.

To accelerate technology development in active controls, the Douglas Aircraft Company has built and tested an aeroelastic model of a DC-10 derivative wing equipped with an active control system (refs. 1 and 2). Because of an extensive background in active controls technology within NASA, cooperative studies were initiated between Douglas and NASA to evaluate alternate control laws that could be designed and tested on the aeroelastic model. The scope of this cooperative study was to apply control-law design methods developed by NASA to a realistic transport with engines on the wing.

The purpose of this paper is to report on two control laws that were designed at NASA for the aeroelastic model and to present results of wind-tunnel tests used to evaluate their performance. The design objective was to synthesize control laws that would demonstrate at least a 20-percent increase in flutter speed above that of the passive wing. The predicted sensitivity of the control laws to both gain and phase is compared with experimental data. In addition, a brief description of the synthesis methodology is presented.

Although not designed to reduce gust loads, it was determined by analysis prior to the wind-tunnel tests that one of the control laws was also effective in reducing wing bending moments due to turbulence. The analysis which predicted the reduction in wing bending moment was performed using DYLOFLEX, a computer program system for dynamic loads analyses of flexible airplanes with active controls (refs. 3 and 4). To verify that the control law would, in fact, alleviate gust loads, turbulence-response experiments were added to the wind-tunnel test plan. A comparison of measured and predicted turbulence responses is presented.

SYMBOLS

a   control-law gain parameter

b   span, m

f   frequency, Hz

$F(s)$ form of control law implemented on analog computer

g   acceleration in gravitational units ($1g = 9.8$ m/sec^2)

K_g fraction of nominal gain

K_p phase-control-filter gain

s Laplace variable

V velocity

V_f velocity at flutter

w_g vertical gust velocity

$\ddot{z}$ feedback acceleration at 88-percent wing semispan station

δ_a control-surface deflection

δ_c control-law command to actuator

ζ damping coefficient

ζ_3 primary-flutter-mode damping coefficient

ζ_{max}, ζ_{min} maximum and minimum damping coefficient, respectively

ζ_n damping coefficient associated with control law

ρ air density

σ_{M_b} root-mean-square value of bending moment

σ_{w_g} root-mean-square value of vertical gust velocity

τ phase-control-filter time constant

ϕ phase angle, deg

ϕ_m phase margin

$\Phi_{M_b}(f)$ power spectral density function of bending moment

$\Phi_{w_g}(f)$ power spectral density function of vertical gust velocity

ω circular frequency

ω_n circular frequency associated with control law

Abbreviations:

E.A.   elastic axis

frf   frequency response function

psd   power spectral density

rms   root mean square

     Dots over symbols denote derivatives with respect to time.

WIND-TUNNEL MODEL AND ANALYSIS METHODS

The model used in this investigation is an aeroelastically scaled semispan model of a derivative DC-10 wing which has approximately a 15.5-percent span increase over the standard DC-10 wing. The model is cantilevered from the tunnel wall and is equipped with a hydraulically actuated outboard aileron, which is used as an active control surface. A photograph of the model mounted in the wind tunnel is presented in figure 1; the model geometry is given in figure 2.

Figure 1.- DC-10 derivative wing in Douglas Low-Speed Wind Tunnel at Long Beach.
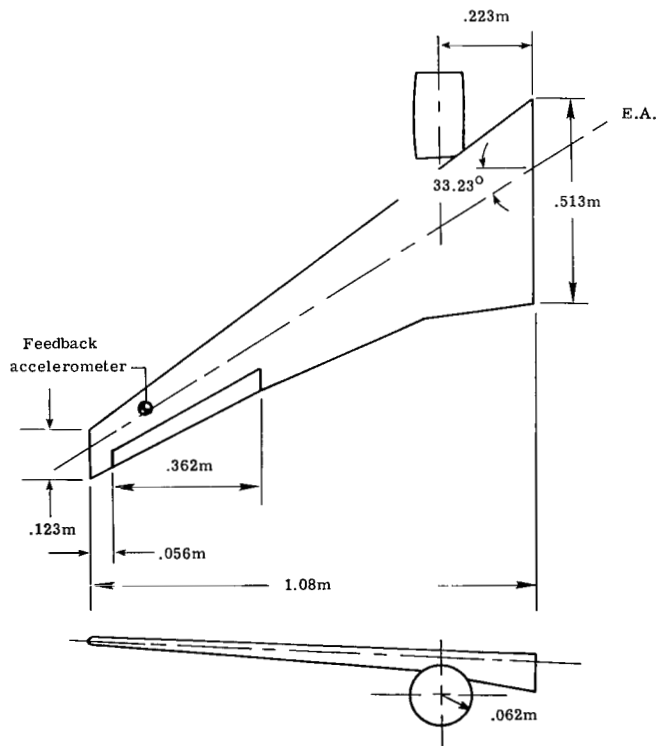

Figure 2.- Model geometry.

Structure

The wing is of conventional spar and pod construction; that is, an aluminum spar is used to provide bending and torsional stiffnesses. Spanwise sections or pods are constructed of balsa wood to provide aerodynamic contours. The engine is represented by a flow-through nacelle and is attached to the wing spar with a beam that simulates the stiffness of the engine pylon and provides the desired degrees of freedom. Although the model is designed to simulate different fuel conditions (through the addition of mass to the wing), all the present studies were performed for the zero-fuel condition. For aeroelastic analysis purposes, the first 10 calculated elastic mode shapes, frequencies, and generalized masses were provided by Douglas Aircraft Company (ref. 2). In addition, NASA was provided with the results of a ground vibration test which were used to compare measured and calculated modal frequencies and node lines for the first eight modes. These results are presented in figure 3. All modes except the first three were assumed to have a damping coefficient ζ of 0.01. Using ground vibration test data, the damping coefficients in the first three modes were estimated to be 0.0060, 0.0005, and 0.0035, respectively.

Control Surface and Actuator

The model is equipped with a trailing-edge control surface which is located between the 66.2-percent and 95.5-percent semispan stations and is 25.0 percent of the local wing chord. The control surface is driven by an electrohydraulic servo-actuator system. The servo actuator serves two purposes: for no external command it fixes the control-surface position relative to the wing in the faired position (for passive testing); and for time varying inputs, it provides control surface motion in a manner dictated by the control law. Maximum control deflection is approximately ±15°.

The servo-actuator system is described in reference 2. Briefly, the actuator consists of a closed compartment separated into two chambers by a self-sealing rotary vane attached to a shaft. The shaft is rotated by applying a differential hydraulic pressure between the two chambers. One end of the shaft is attached to the control surface and the other end is attached to a rotary potentiometer which measures angular rotation.

Because of problems in the actuator hardware, wind-tunnel tests on the NASA-developed control laws were performed during two different time periods. In the time interval between the tests, the actuator hardware was modified to improve its reliability. The modifications resulted in differences in the response characteristics of the actuator. Prior to both wind-tunnel entries, the actuator frequency response was experimentally measured. For analysis purposes, the measured frequency responses were approximated by a transfer function in the Laplace plane. The measured and approximated frequency responses of the actuator for the two wind-tunnel entries are presented in figure 4. At the basic flutter frequency of 12 Hz the measured phase
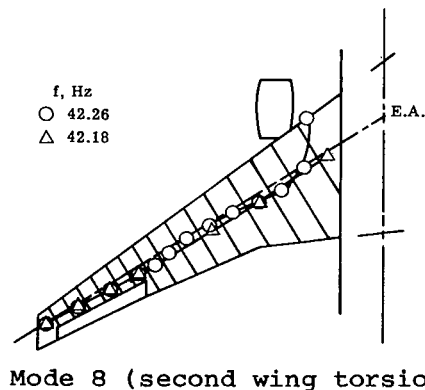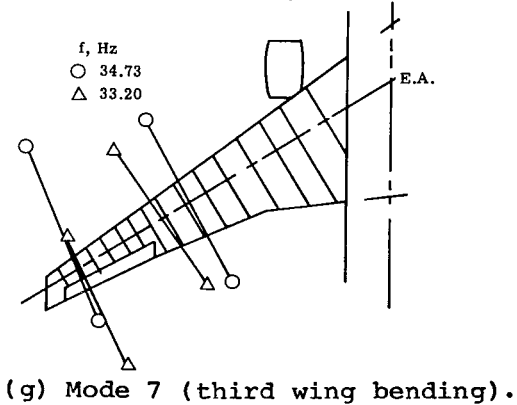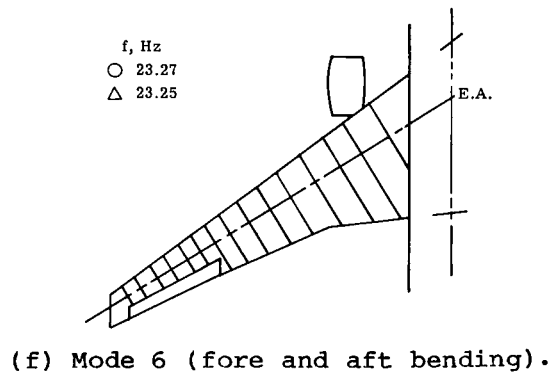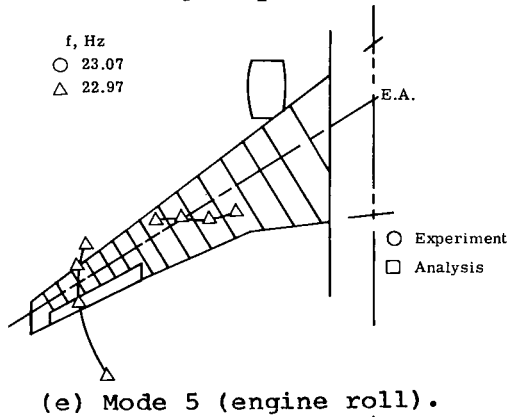
4

(a) Mode 1 (first wing bending).

(b) Mode 2 (engine yaw).

(c) Mode 3 (first wing torsion and engine pitch).

(d) Mode 4 (second wing bending).

(e) Mode 5 (engine roll).

(f) Mode 6 (fore and aft bending).

(g) Mode 7 (third wing bending).
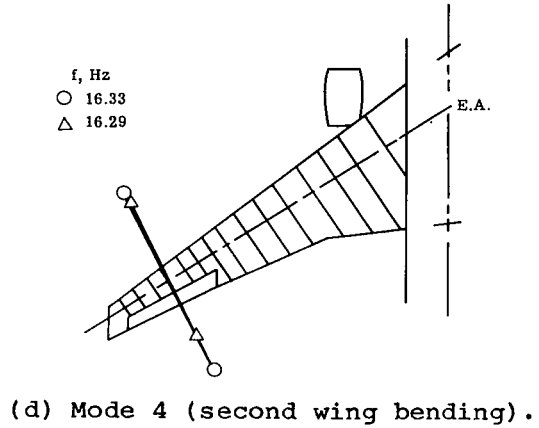
(h) Mode 8 (second wing torsion).
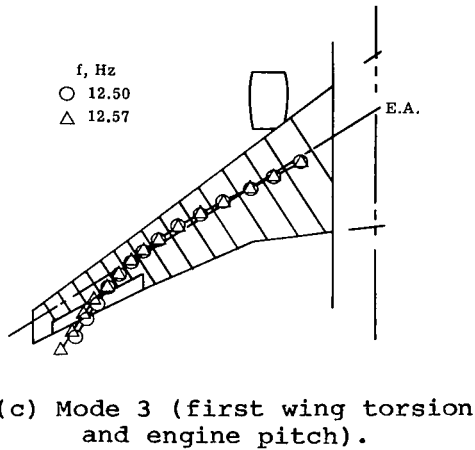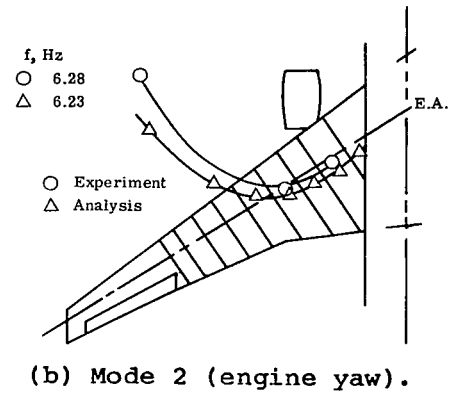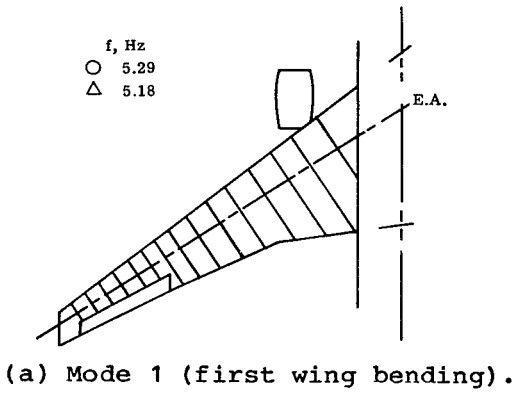
Figure 3.- Node lines and frequencies for first eight structural modes.
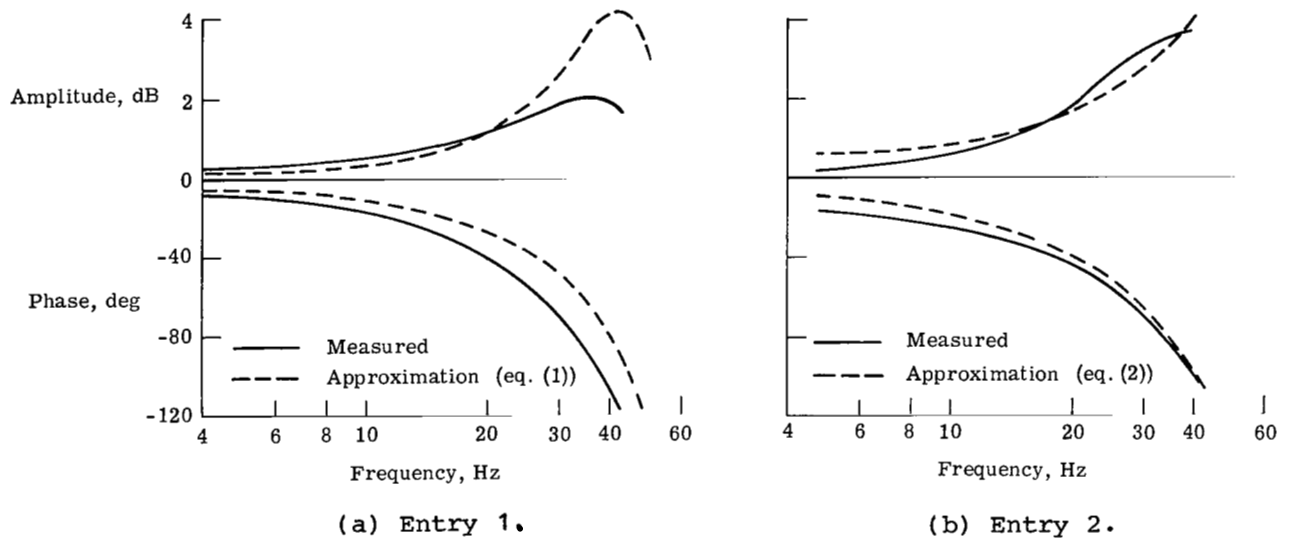
(a) Entry 1. (b) Entry 2.

Figure 4.- Measured and approximated frequency responses of actuator.

lag of the actuator is approximately 7° greater during the second tunnel entry. The equations used to approximate the measured frequency responses are

Entry 1:

$$\frac{\delta_a}{\delta_c} = \frac{0.6226 \times 10^8}{(s^2 + 180.9s + 90958.2)(s + 684.87)} \frac{deg}{deg} \tag{1}$$

Entry 2:

$$\frac{\delta_a}{\delta_c} = \frac{1.1105 \times 10^{10}}{(s^2 + 87.51s + 138406)(s^2 + 351.6s + 75696)} \frac{deg}{deg} \tag{2}$$

Instrumentation

Figure 5 presents a sketch of the wing planform illustrating the location and type of instrumentation used for the experimental investigation. The dashed line represents the wing elastic axis. Strain-gage bridges are located in pairs at approximately the 48-percent and 78-percent semispan stations. The inboard bridge in each pair was aligned to measure torsion about the wing spar; and the outboard bridge in each pair was aligned to measure the bending moment about an axis in the plane of the wing which is perpendicular to the wing spar. An accelerometer is located on the wing at the 88-percent semispan station. This accelerometer is used to monitor the wing motion and to provide a feedback signal for the active control system. A rotary potentiometer is used to measure aileron deflection.
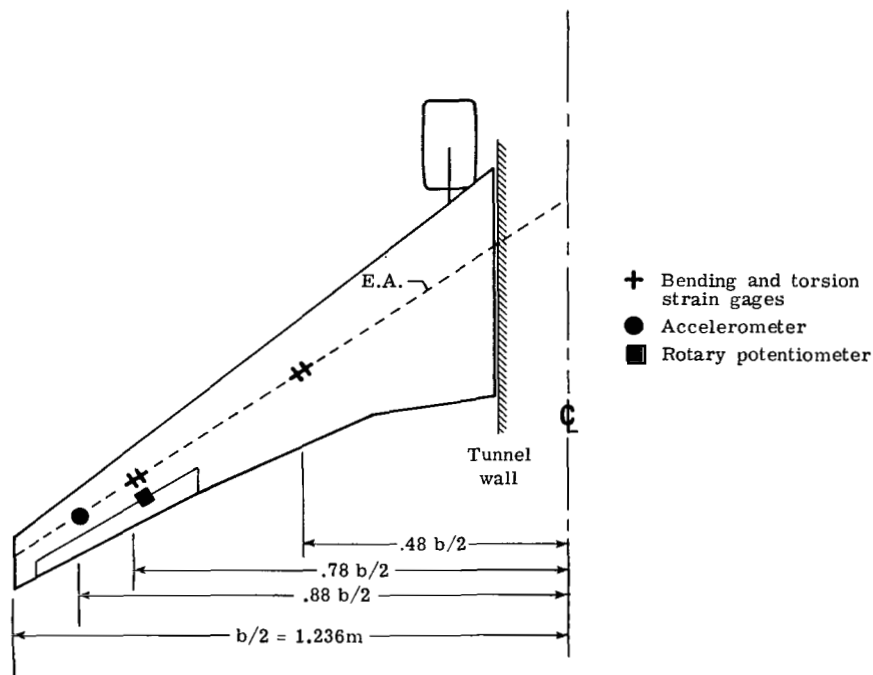
6

Figure 5.- Model instrumentation.

Analysis Methods

For stability analysis the unsteady aerodynamics are combined with the structure and the control-surface frequency response function (for closed-loop analysis) by approximating the variation in frequency of the unsteady aerodynamics with a rational polynomial in the variable s. Unsteady aerodynamics for the first 10 calculated structural modes and a control-surface rotation mode are computed using a doublet lattice method. A description of the analysis methods used to calculate the open- and closed-loop flutter characteristics is presented in appendix A.

Predicted turbulence responses were computed using DYLOFLEX, a system of computer programs which performs dynamic loads analyses of flexible airplanes with active controls. The equations of motion in DYLOFLEX are formulated through a modal approach using Lagrange's equations of motion. The loads equations are developed using summation of forces. DYLOFLEX requires the following information to perform an analysis: mode shapes, generalized mass and stiffness matrices, lumped masses, static moments, and moments of inertia. This information, as well as the power spectral density functions of the vertical component of tunnel turbulence at three different tunnel speeds, was supplied to NASA by Douglas Aircraft. A description of the DYLOFLEX analysis method is presented in appendix A.

WIND-TUNNEL TESTS

All experimental studies were conducted in the Douglas Low-Speed Wind Tunnel at Long Beach, California. The tunnel is a closed-circuit, continuous-flow facility with a test section 0.96 m by 1.37 m. The tunnel operates at atmospheric pressures at speeds up to approximately 67 m/sec, depending on tunnel blockage. During the flutter tests, both the damping of the flutter mode and the flutter velocity were

7

measured. The damping was estimated by calculating the logarithmic decrement of the response of the wing to a pulsed input. (The pulsed input was introduced to the model through small-diameter cables which attached to the wing tip and engine nacelle.) The damping is calculated by the following equation:

$$\zeta = \frac{1}{2\pi n} \ln \frac{A_1}{A_2} \qquad (3)$$

where

n   number of cycles between A_1 and A_2

A_1 initial amplitude

A_2 amplitude of nth cycle

    To perform the turbulence-response wind-tunnel tests, turbulence had to be created in the test section. The turbulence was created by installing a "canvas banner" across the width of the tunnel about 5 m upstream of the test section. The flapping of the banner, while the tunnel is running, creates random fluctuations in velocity. A description of the nature of the wind-tunnel turbulence and the approximations used to analytically represent the turbulence are presented in appendix B. The banner was removed for flutter testing.

    The model was tested previously by McDonnell Douglas Corporation. (See refs. 1 and 2.) The NASA tests were performed during two different tunnel entries. The second entry was added because of a failure in the servo actuator which caused the first test to be halted prematurely. Because of this failure, the first entry was devoted exclusively to flutter testing. The second entry involved both turbulence and flutter testing in roughly equal amounts.

PASSIVE WING FLUTTER CHARACTERISTICS

    The initial phase of testing during both entries was devoted to measuring the passive flutter characteristics of the wing. The purpose was (1) to validate the mathematical model used to predict the passive flutter characteristics (and also used to synthesize the control laws) and (2) to ensure that the model characteristics had not changed between tunnel tests.

Analysis

    A root locus of the eigenvalues of the characteristic flutter equation for the passive wing as a function of velocity is presented in figure 6 (arrows indicate increasing velocity). Each curve corresponds to a structural degree of freedom. The passive wing is predicted to exhibit two distinct flutter modes. The first (primary flutter mode) occurs at a velocity of 46.93 m/sec and is characterized by a coupling between first wing bending (mode 1) and first wing torsion and engine pitch (mode 3). The flutter frequency is approximately 78.5 rad/sec (12.5 Hz). The higher frequency instability involves primarily second wing torsion (mode 8) and is stable to a relatively high velocity of 67.1 m/sec. The corresponding flutter frequency is approximately 151 rad/sec (24 Hz).
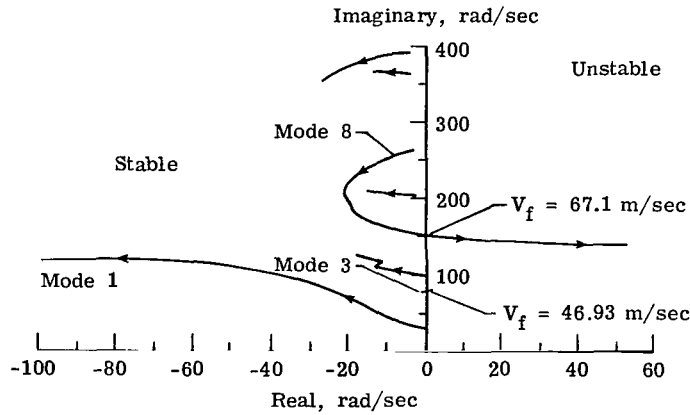
Figure 6.- Velocity root locus for passive wing. (Arrows indicate
increasing velocity.)

Experiment

Both the damping of the primary flutter mode (mode 3 in fig. 6) at subcritical
speeds and the flutter velocity were measured. A comparison of measured and pre-
dicted flutter mode damping (mode 3) is presented in figure 7. The predicted flutter
velocity is 3 percent lower than the measured velocity of 48.35 m/sec. Estimates of
subcritical damping are quite reasonable. On the basis of these results, it appears
that the analytical predictions compare reasonably well with experimental data.
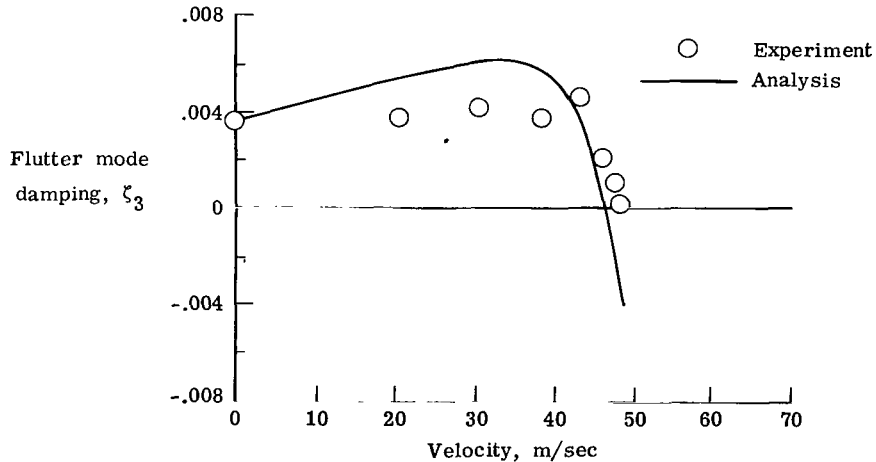

Figure 7.- Comparison of measured and predicted flutter mode damping
for passive wing.

CONTROL LAWS

The objective of the study was to design and test control laws capable of demon-
strating at least a 20-percent increase in flutter speed over that of the passive
wing. The design point selected for control-law synthesis was V = 56.32 m/sec
(1.2 × Calculated flutter velocity). Two control laws, one patterned after the

aerodynamic energy method and the other after optimal control theory, were designed. (For an earlier application of these methods, see ref. 5.) Before proceeding with a description of each synthesis method, those elements common to both control laws will be described.

Early in the design of the NASA control laws, it was determined that the feedback accelerometer should be moved inboard from the tip region, where it was located for the tests described in reference 1. It was shown in reference 1 that an increase in system gain would be required to make the control law more effective in the primary wing flutter mode (12.5 Hz). This increased gain, however, destabilizes the third wing bending mode, resulting in a 34.7-Hz instability. (See fig. 12 of ref. 1.) This same trend was evident in the early design cycle of the present study. To decouple this higher frequency mode from the flutter suppression system, the location of the feedback accelerometer was moved inboard to a point close to the node line associated with the third bending mode. Both control laws used this location for the feedback accelerometer.

In order to eliminate any static problems, such as a static deflection of the control surface due to a drift in the accelerometer amplifier, a washout filter of the form $s/(s + 5)$ was added to the feedback loop prior to control-law synthesis. In addition, both control laws were designed using the actuator transfer function defined by equation (1).

Synthesis

Control law 1.- The form of control law 1 was patterned after the aerodynamic energy method (ref. 6) and used the following transfer function for design purposes:

$$\frac{\delta_a}{\ddot{z}} = \frac{\delta_c}{\ddot{z}} \frac{\delta_a}{\delta_c} \tag{4}$$

where δ_a/δ_c is defined by equation (1) and the control law is defined by

$$\frac{\delta_c}{\ddot{z}} = \frac{a}{s^2 + 2\zeta_n \omega_n s + \omega_n^2} \frac{s}{s + 5}$$

The design process, using the aerodynamic energy method, involves determining the values of a, ζ_n, and ω_n which minimize the control-surface response to turbulence. However, for the flutter-testing portion of these tests a spectrum of tunnel turbulence was not available. The banner used to create turbulence was used only for the load-measurement portion of the tests and was removed for flutter testing. Therefore, the design process was modified to determine the values of a, ζ_n, and ω_n which provide the required increase in flutter speed with acceptable gain and phase margins across the velocity range. Based on previous experience with similar systems, gain margins of ±6 dB and phase margins of ±30° were selected. The values of a, ζ_n, and ω_n which satisfied these requirements were determined by trial and error.

An example of the effect of varying the gain parameter a on the primary flutter mode damping is presented in figure 8. For this case the parameters ζ_n
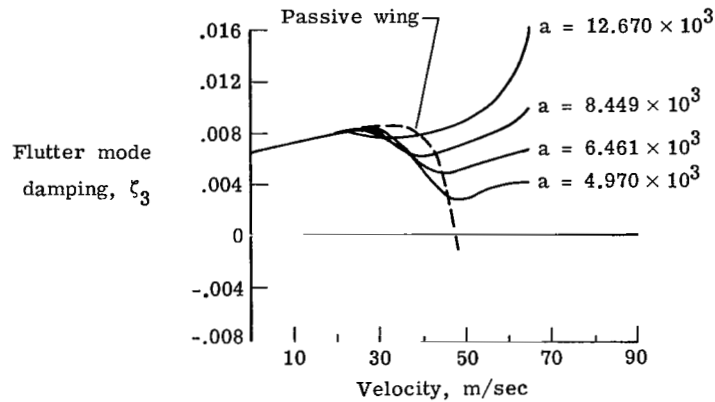
Figure 8.- Predicted variation in flutter mode damping with parameter a.

and ω_n were fixed at 1.0 and 25 rad/sec, respectively, as previously determined by trial and error. (The actuator transfer function is defined by eq. (1).) The dashed line represents the predicted passive wing damping characteristics in this mode. (Note that the value of damping at $V = 0$ in fig. 8 is larger than that presented previously in fig. 7. During control-law synthesis, the damping in mode 3 was erroneously assumed to be 0.0064. The effect of this difference on the design is discussed later.) It can be seen from figure 8 that the closed-loop damping at velocities below the passive wing flutter speed has been reduced, as compared with the damping of the passive wing. This trend occurred for all combinations of a, ζ_n, and ω_n that were analyzed. Since the level of damping in the passive wing flutter mode is initially very low ($\zeta_{max} \approx 0.0085$), it was decided that a constraint based on damping would be added to the design. For nominal gain, the constraint was that the minimum closed-loop damping below the passive wing flutter speed could not be lower than the damping at zero velocity (i.e., $\zeta_{min} \geq 0.0064$). The curve (fig. 8) represented by $a = 8.449 \times 10^3$ came the closest to meeting this design requirement.

Figure 9 presents a Nyquist diagram of control law 1 at the design point $V = 56.32$ m/sec. Arrows indicate increasing frequency. Gain margins of -8.1 dB
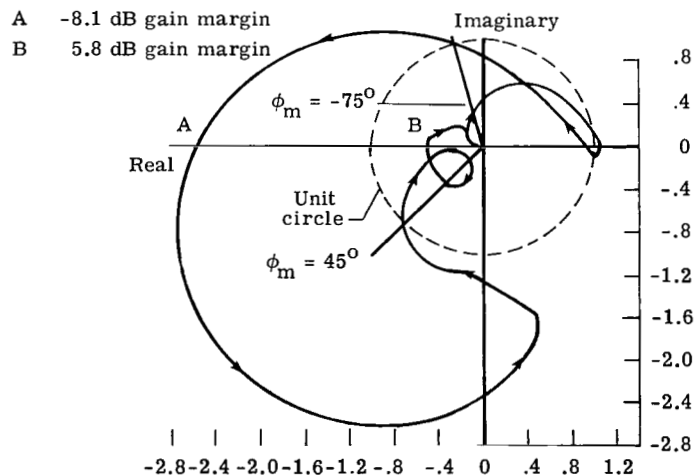

Figure 9.- Nyquist diagram for control law 1 at V = 56.32 m/sec.
(Arrows indicate increasing frequency.)

and 5.8 dB along with phase margins of −75° and 45° are indicated. The following transfer function represents the control law (which includes the washout filter) that was implemented on the model:

$$\frac{\delta_c}{\ddot{z}} = \frac{8.449 \times 10^3}{s^2 + 2(1.0)25s + 25^2} \frac{s}{s + 5} \frac{\text{deg}}{g} \tag{5}$$

Control law 2.– Control law 2 was designed to meet the same gain and phase margins (±6 dB and ±30°) used in the design of control law 1. However, the minimum damping constraint was not used. The synthesis technique used to design the control law is based on the method described in reference 5. This method is used to design a reduced-order control law from the results of a full-state feedback optimal control law. The method requires that the open-loop frequency response of the reduced-order control law closely match the open-loop frequency response of the full-state optimal control law over a finite frequency range.

The form of the control law initially examined was identical to control law 1; that is,

$$\frac{\delta_c}{\ddot{z}} = \frac{a}{s^2 + 2\zeta_n\omega_n s + \omega_n^2} \frac{s}{s + 5} \tag{6}$$

An optimization algorithm was then used to find the values of a, ζ_n, and ω_n that minimize the difference between the open-loop frequency response function using equation (6) and the optimal open-loop frequency response function at the design point. The optimization algorithm drove ζ_n and ω_n to zero, resulting in

$$\frac{\delta_c}{\ddot{z}} = \frac{a}{s^2} \frac{s}{s + 5} \tag{7}$$

This control law results in high system gain at low frequency; therefore, the s^2 term was changed to $(s + 10)^2$, resulting in the following trial control law:

$$\frac{\delta_c}{\ddot{z}} = \frac{a}{(s + 10)^2} \frac{s}{s + 5} \frac{\text{deg}}{g} \tag{8}$$

where $a = 4.450 \times 10^3$. A Nyquist diagram of this trial control law at the design point is presented in figure 10, which shows that the gain and phase margins at the design point are acceptable. The flutter mode damping across the velocity range, using this control law, is presented in figure 11. Note that the control law drives the wing unstable below the passive wing flutter speed. The instability is attributed to the fact that the optimal control law at the design point requires 180° of phase lag. This amount of phase lag at velocities below the passive wing flutter speed promotes the instability. A Nyquist analysis was performed at the instability velocity. This analysis provided a graphical means to determine how the gain and phase of the control law should be changed to stabilize the system. The Nyquist analysis indicated that the addition of 30° of phase lead (at 12 Hz) to equation (8) eliminates the instability. However, the addition of this phase lead significantly reduces the positive gain margin.
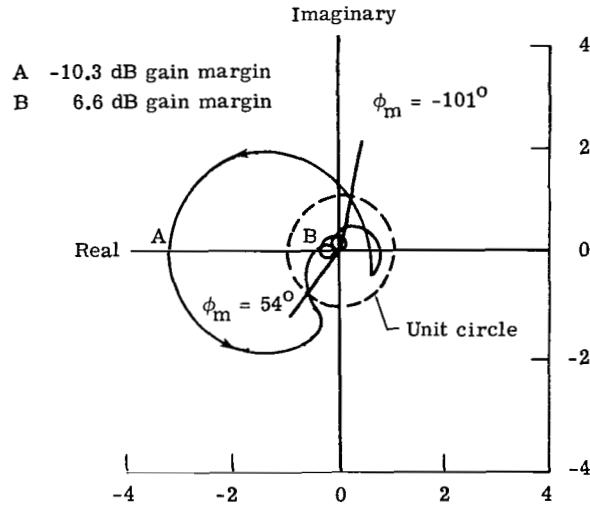
Figure 10.- Nyquist diagram for trial control law 2 at V = 56.32 m/sec.
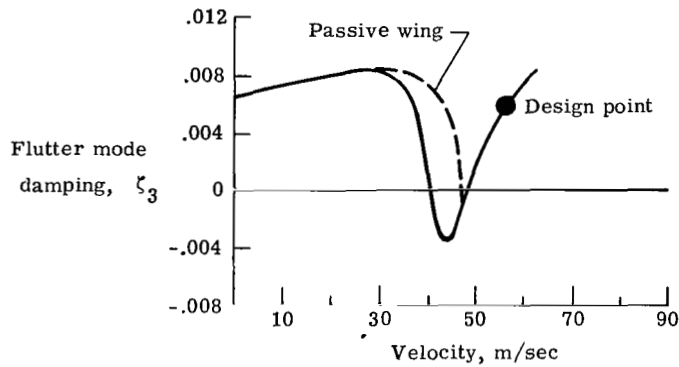(Arrows indicate increasing frequency.)

Figure 11.- Predicted variation in flutter mode damping with velocity
for trial control law 2.

The terms that were added to improve both the flutter mode damping and gain margins of the control law are as follows. The first term

$$\frac{s - 20}{s + 20}$$

is a filter which provides approximately 30° of phase lead at 12 Hz to improve flutter mode damping near the passive wing flutter speed. The second term

$$\frac{s^2 + 7.2s + 144}{s^2 + 19.2s + 144}$$

is a notch filter at approximately 2 Hz to improve the positive gain margin resulting from the introduction of the first term. The third term

$$\frac{628^2}{(s + 628)^2}$$

is a 100-Hz double-pole filter to attenuate high-frequency inputs. The fourth term is an increase in a (from 4.450×10^3 to 6.640×10^3) to compensate for a decrease in the negative gain margin resulting from the introduction of the first, second, and third terms. The resulting control law (control law 2) can be written as

$$\frac{\delta_c}{\ddot{z}} = \frac{6.640 \times 10^3}{(s + 10)^2} \frac{s}{s + 5} \frac{s - 20}{s + 20} \frac{s^2 + 7.2s + 144}{s^2 + 19.2s + 144} \frac{(628)^2}{(s + 628)^2} \frac{deg}{g} \tag{9}$$

The Nyquist diagram at the design point using equation (9) is presented in figure 12. Comparison of these results with those in figure 10 shows that at the
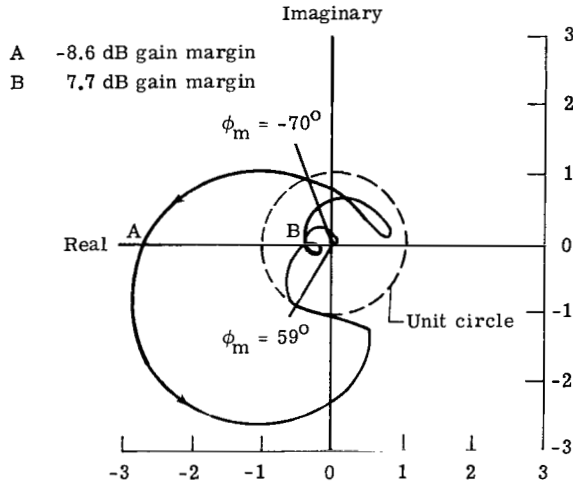

Figure 12.- Nyquist diagram for control law 2 at $V = 56.32$ m/sec. (Arrows indicate increasing frequency.)

design point, the stability margins have decreased but are still in the acceptable region. The flutter mode damping as a function of velocity is presented in figure 13. Comparison of these results with those of figure 11 shows the improvement
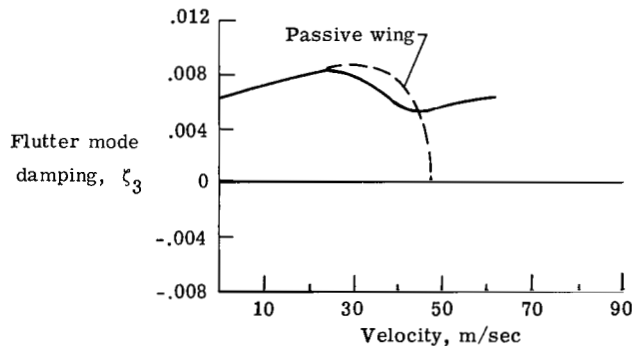

Figure 13.- Predicted variation in flutter mode damping with velocity for control law 2.

in flutter mode damping and shows that the wing remains stable throughout the velocity range of interest.

Implementation

A simplified block diagram of the active control system is presented in figure 14. Both control laws were programmed on an analog computer. The quantity w_g represents a disturbance input from the vertical component of wind-tunnel turbulence.

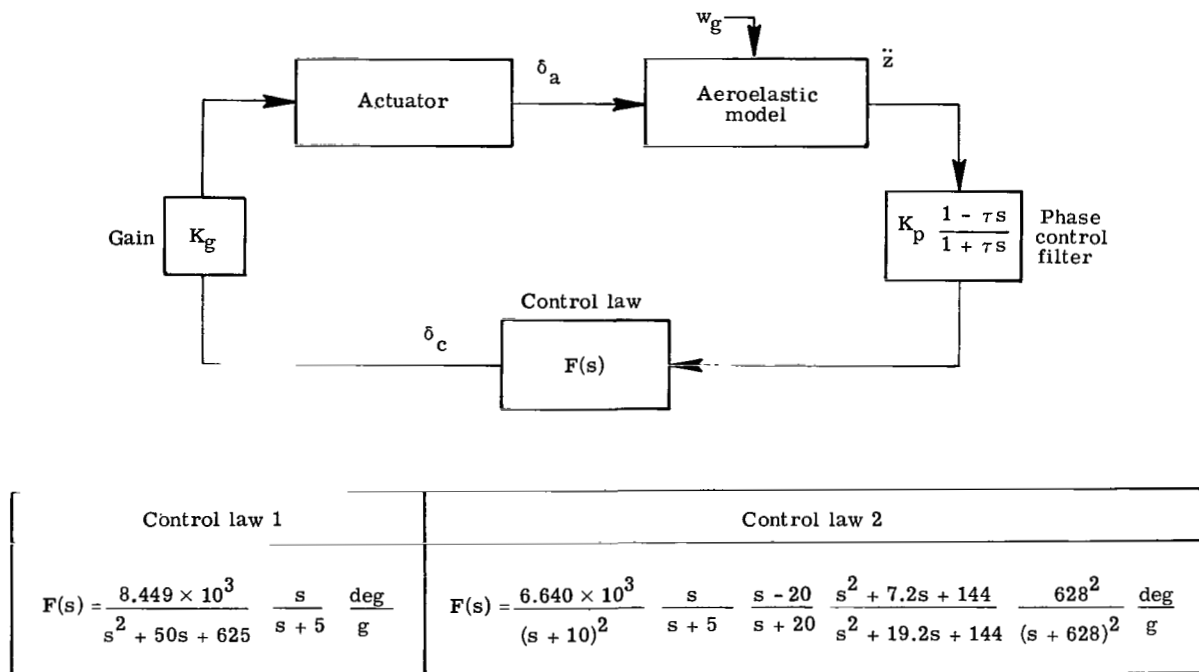| Control law 1	Control law 2
$F(s) = \dfrac{8.449 \times 10^3}{s^2 + 50s + 625} \dfrac{s}{s + 5} \dfrac{deg}{g}$	$F(s) = \dfrac{6.640 \times 10^3}{(s + 10)^2} \dfrac{s}{s + 5} \dfrac{s - 20}{s + 20} \dfrac{s^2 + 7.2s + 144}{s^2 + 19.2s + 144} \dfrac{628^2}{(s + 628)^2} \dfrac{deg}{g}$

Figure 14.- Block diagram of active control system.

Vertical acceleration $\ddot{z}$ is measured at the 88-percent wing semispan station. A phase control filter of the form

$$K_p \frac{1 - \tau s}{1 + \tau s} \tag{10}$$

where

$$K_p = 1 \quad \text{for phase lag}$$

$$K_p = -1 \quad \text{for phase lead}$$

is included in the analog computer. By properly choosing the quantities τ and K_p, a phase lead or lag of known amount ϕ is introduced at a given frequency ω (where $s = i\omega$) without changing system gain. The time constant τ is evaluated by the expression

$$\tau = \left\{ \tan\left[(1 - K_p)(45) - \frac{\phi}{2} \right] \right\} \omega \tag{11}$$

15

where ϕ is in degrees. Nominal phase is $\phi = 0°$ ($\tau = 0$; $K_p = 1$). The transfer function $F(s)$ defines the control law being tested (including washout filter). The quantity K_g is a normalized gain. It is continuously variable and has a value of 1 for nominal gain and a value of 0 for the system off. Gain K_g and phase ϕ were varied during the wind-tunnel tests.

PREDICTED PERFORMANCE

During the first entry, both control laws were tested to establish their effects on increasing the flutter speed. During the second entry, control law 1 was thoroughly evaluated in terms of flutter and gust loads. Control law 2 was not tested during the second entry. As stated previously, both control laws were designed assuming the damping in mode 3 to be $\zeta = 0.0064$. It was determined that the damping in this mode was actually 0.0035. The predicted performance takes into account the actuator frequency response applicable to the test entry and the corrected value of damping in mode 3.

Flutter

Control law 1.- Figure 15 presents a Nyquist diagram of control law 1 with the lower value of damping in mode 3; figure 16 presents the effects of lower damping and the modified actuator. A summary of these results is presented in the following table:

Description	Gain margin, dB		Phase margin, deg		ζ_3	Actuator defined by
	Negative	Positive	Negative	Positive		
Pre-test	-8.1	5.8	-75	45	0.0064	Eq. (1)
Entry 1	-5.6	4.3	-62	31	.0035	Eq. (1)
Entry 2	-6.8	1.5	-78	12	.0035	Eq. (2)

The predominant effect of reducing ζ_3 is to decrease the gain and phase margins. The modified-actuator transfer function tends to rotate the Nyquist diagram clockwise about the origin. This produces a significantly lower positive phase margin and a lower positive gain margin. These results indicate that for this model, the damping coefficient in the flutter mode and the actuator transfer function play a significant role in establishing the stability margins for the control law. Since the bulk of the experimental data on control law 1 was gathered during the second tunnel entry, the predicted results for this case are presented (i.e., $\zeta_3 = 0.0035$ and actuator transfer function defined by eq. (2)).
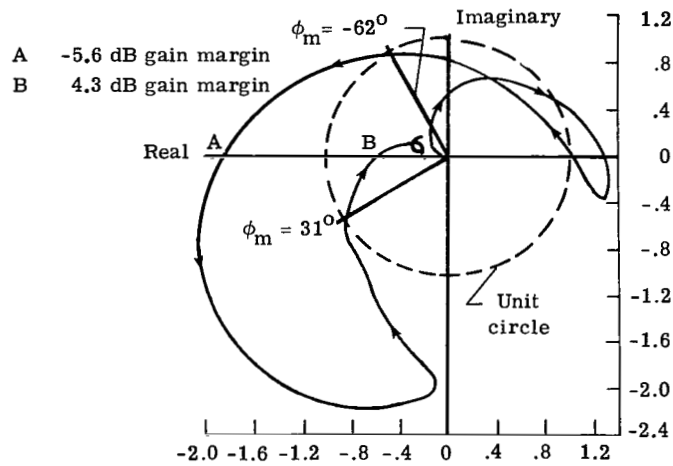
Figure 15.– Nyquist diagram for control law 1 with $\zeta_3 = 0.0035$ and actuator defined by equation (1). (Arrows indicate increasing frequency.)
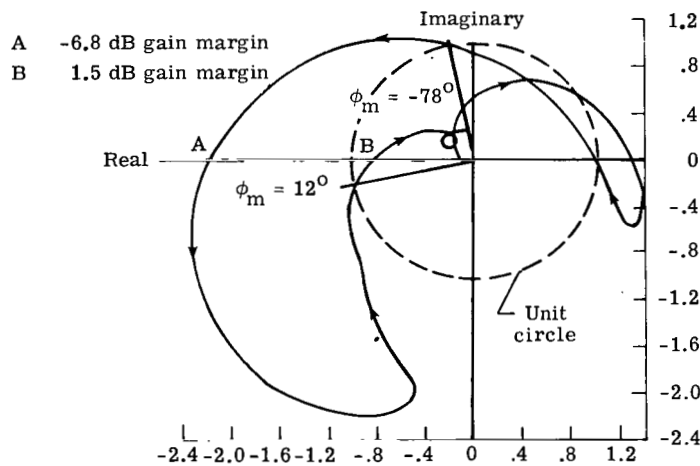

Figure 16.– Nyquist diagram for control law 1 with $\zeta_3 = 0.0035$ and actuator defined by equation (2). (Arrows indicate increasing frequency.)

Using the control law defined by equation (5) and the actuator transfer function defined by equation (2), a stability calculation was performed. The results of this calculation are presented in figure 17 as a closed-loop root locus which illustrates the variation of the system modal eigenvalues with velocity. In comparing these results with those of the passive system (fig. 6), note the following: (1) the flutter mode (mode 3) is stabilized to the maximum velocity analyzed (V = 76.2 m/sec); (2) mode 8 is unstable at V = 0, becomes stable at low values of V, and then goes unstable once again at approximately the same value of V as for the passive wing; (3) two new modes associated with the feedback filter and actuator are generated; and (4) all other modes are basically unaffected by the active control system.
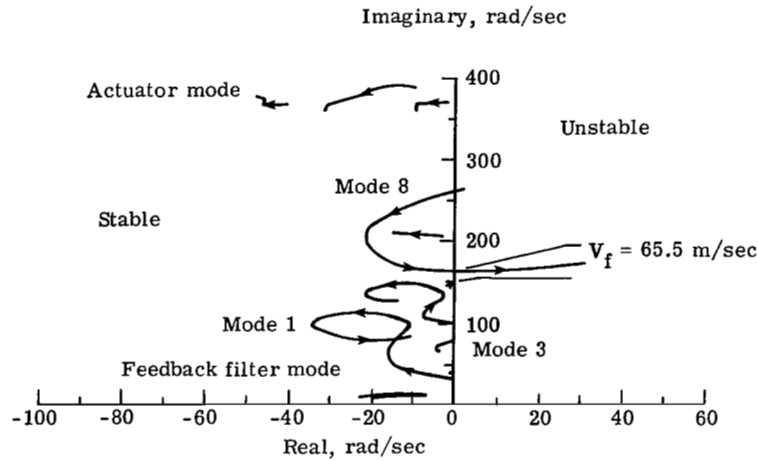
Figure 17.- Closed-loop root locus for control law 1 with $\zeta_3 = 0.0035$ and actuator defined by equation (2). (Arrows indicate increasing velocity.)

The variation in flutter mode damping ζ_3 with velocity at various values of normalized gain K_g and phase is presented in figure 18. The phase angle ϕ refers to the value of the phase control filter (eq. (11)) evaluated at 12 Hz. The damping characteristics of the nominal control law ($\phi = 0°$; $K_g = 1.0$) are presented in figure 18(a). All analyses were performed to a maximum velocity of 76.2 m/sec. However, the curves in figure 18 are terminated at a lower value of velocity when a mode other than mode 3 goes unstable. Figures 18(b) and 18(c) follow the same format, but for phase angles of -20° and 20°, respectively.
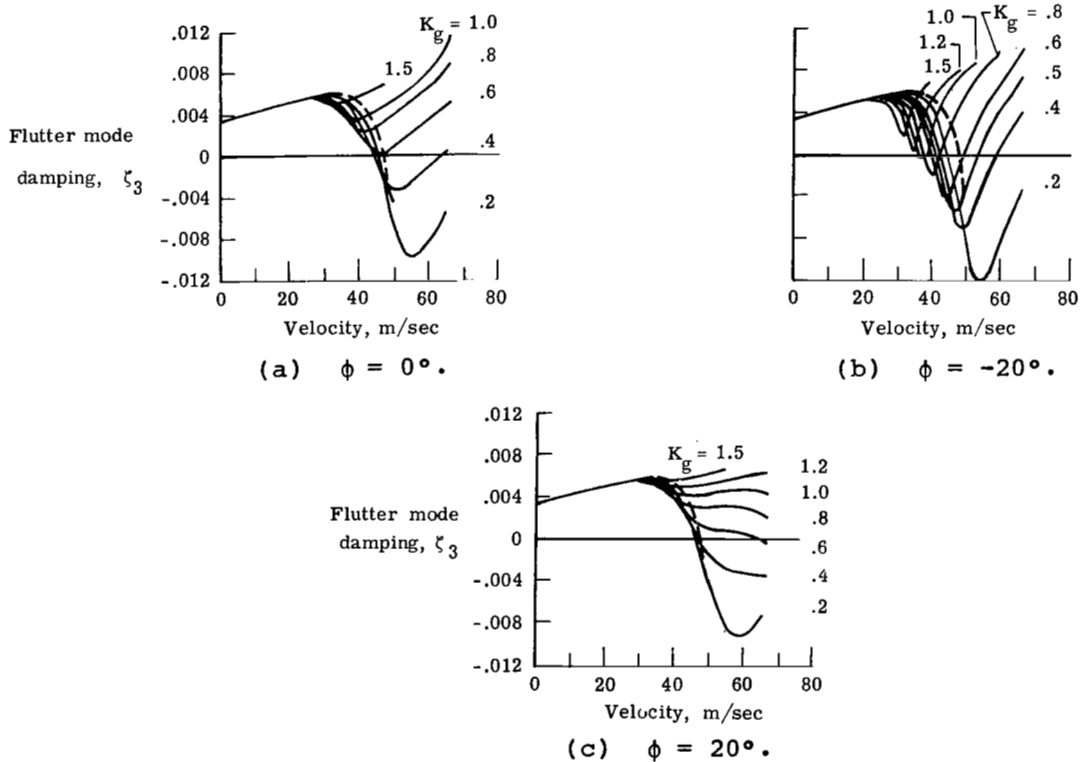

(a) $\phi = 0°$.

(b) $\phi = -20°$.

(c) $\phi = 20°$.

Figure 18.- Variation in flutter mode damping with gain and phase for control law 1. (Passive wing is denoted by dashed lines.)

18

From figure 18(a), it can be seen that the nominal control law provides an increase in flutter velocity in excess of 20 percent. As mentioned previously, however, because of the decrease in damping in the flutter mode and the actuator modifications, the control law does not exhibit either the ±6 dB gain margins or the ±30° phase margins. For all phase angles analyzed, the control law degrades the flutter mode damping at low velocities. This degradation is less for the positive phase angles and greater for the negative phase angles. As velocity is increased, this effect is reversed. These trends with phase angle for the nominal control law are illustrated in figure 19. The effect of phase angle on system performance is attributed to significant phase variations in the response of the wing to control-surface motions that are experienced as the velocity is increased. This fact, coupled with the extremely low value of damping in the flutter mode for this wing, results in a control law which is very sensitive to phase variation.
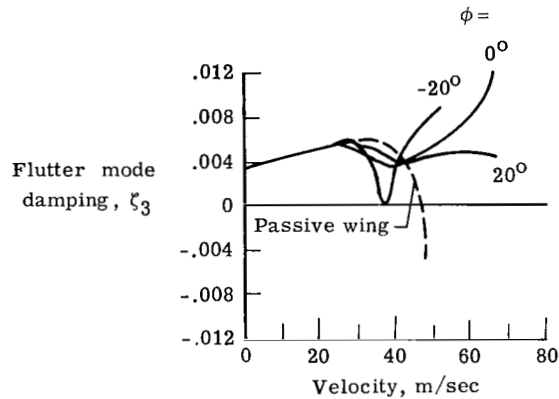
Figure 19.- Variation in flutter mode damping with phase for control law 1. $K_g = 1.0$.

Control law 2.- Experimental data for control law 2 were gathered during the first tunnel entry; therefore, only the predicted results for this case will be presented (i.e., $\zeta_3 = 0.0035$ and actuator transfer function defined by eq. (1)). A closed-loop root locus is presented in figure 20. Comparing the results in figure 20 with those for control law 1 (fig. 17) shows that the locus of flexible-mode eigen-
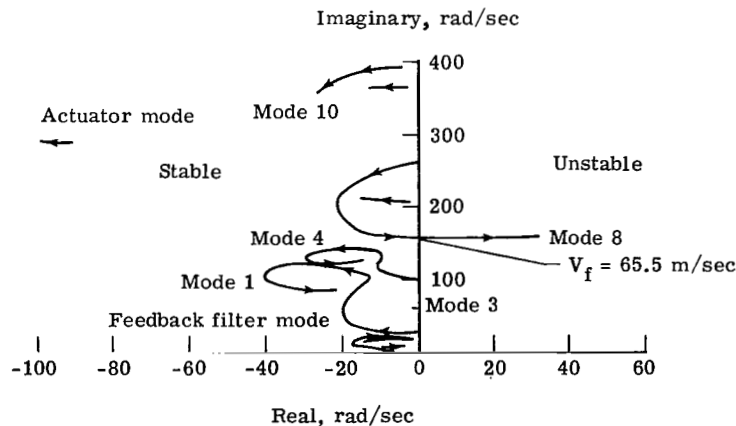
Figure 20.- Closed-loop root locus for control law 2 with $\zeta_3 = 0.0035$ and actuator defined by equation (1). (Arrows indicate increasing velocity.)

values is very similar. The major differences appear to be in the location of the actuator mode and a greater coupling between flexible mode 1 and the feedback filter mode in control law 2. A Nyquist diagram of control law 2 at the design point (V = 56.32 m/sec) is presented in figure 21. The effect of reducing ζ_3 on gain and phase margins can be determined by comparing the results in figure 21 with those in figure 12. The following table summarizes these results:

Description	Gain margin, dB		Phase margin, deg		ζ_3	Actuator defined by
	Negative	Positive	Negative	Positive		
Pre-test	-8.6	7.7	-70	59	0.0064	Eq. (1)
Entry 1	-3.8	4.6	-44	50	.0035	Eq. (1)

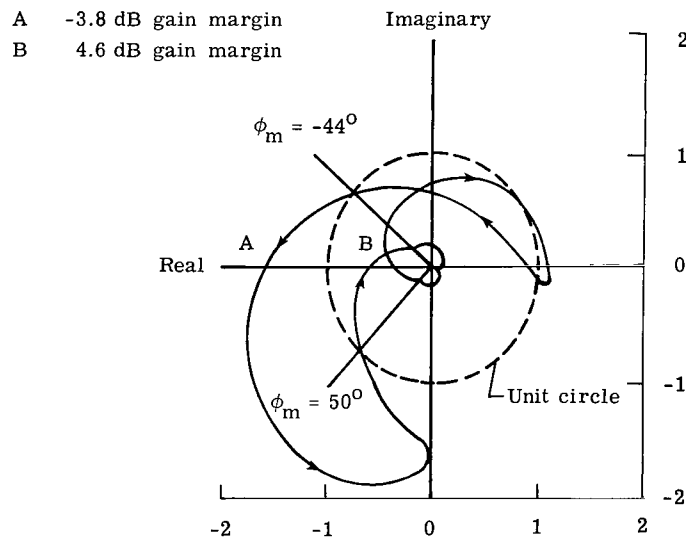A   -3.8 dB gain margin
B   4.6 dB gain margin

Figure 21.- Nyquist diagram for control law 2 with ζ_3 = 0.0035 and actuator defined by equation (1). (Arrows indicate increasing frequency.)

The variation in flutter mode damping ζ_3 with velocity at various values of gain and phase is presented in figure 22. The format for this figure is the same as previously described for control law 1 (i.e., K_g, ϕ, and maximum velocity plotted). The nominal control law provides an increase in velocity above the passive wing flutter speed in excess of 20 percent. The trends with phase angle and gain for control law 2 are similar to those presented for control law 1. However, it should be noted that the phase angles presented in figures 22(b) and 22(c) are for ±10° as compared with ±20° for control law 1. For nominal gain, the variation in flutter mode damping at ϕ = 0°, -10°, and 10° is given in figure 23. Comparison of the flutter mode damping with phase for both control laws (figs. 19 and 23) shows that the effect of phase lead on control law 2 is greater than for control law 1. This is attributed to the fact that control law 1 has a larger negative phase margin at the design point than does control law 2 (-78° compared with -44°). Positive phase introduced by the phase control filter rotates the Nyquist diagram in a counterclockwise direction. Since control law 1 has a larger negative phase margin, phase lead will have less of an effect on the flutter mode. In addition, the minimum level of damping associated with control law 1 is greater than with control law 2. Calculations performed for control law 2 with 20° of phase lead predicted that the closed-loop system would be

(a) $\phi = 0°$.

(b) $\phi = -10°$.
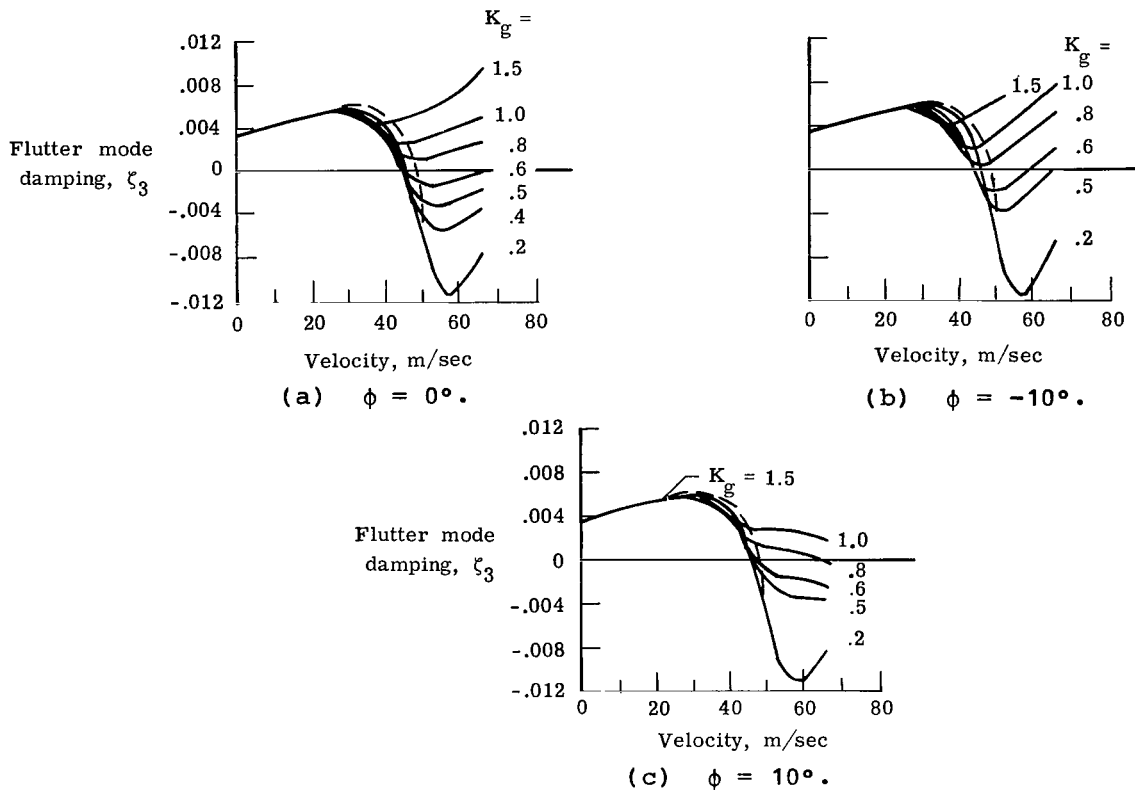

(c) $\phi = 10°$.

Figure 22.- Variation in flutter mode damping with gain and phase for control law 2. (Passive wing is denoted by dashed lines.)
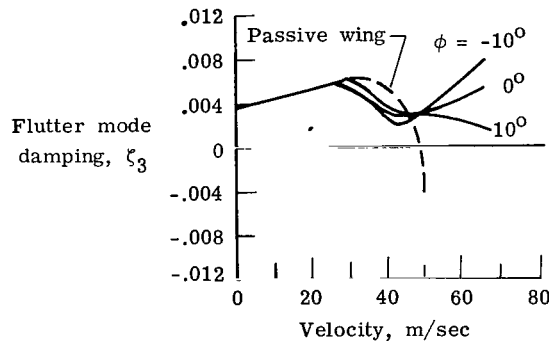

Figure 23.- Variation in flutter mode damping with phase for control law 2. $K_g = 1.0$.

unstable below the 20-percent velocity margins. For all phase angles analyzed, control law 2 degrades the flutter mode damping at low velocities. This degradation is less for the positive phase angles than for the negative angles. As velocity is increased, this trend is reversed.

Gust Response

A power spectral density function of bending moment $\Phi_{M_b}(f)$ for the active control system off at $V = 30.9$ m/sec is presented in figure 24(a). The psd is presented as a log-log plot of bending moment versus frequency. The psd is charac-
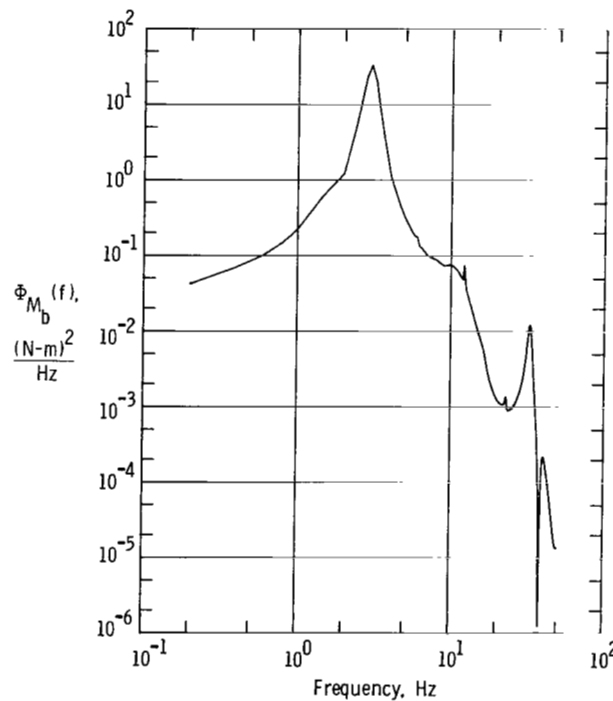
terized by peaks at frequencies of approximately 3.0 Hz and 6.9 Hz (tunnel-turbulence peak and first wing bending peak) and a prominent peak at about 30 Hz (third wing bending). A small peak at 12 Hz is associated with the primary flutter mode. The system-off rms bending moment at $V = 30.9$ m/sec is 3.246 N-m.
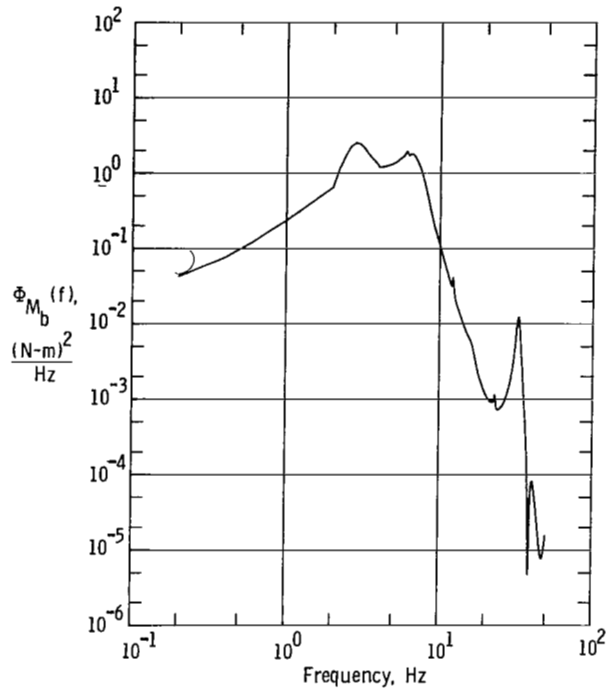
(a) System off; rms = 3.246 N-m.
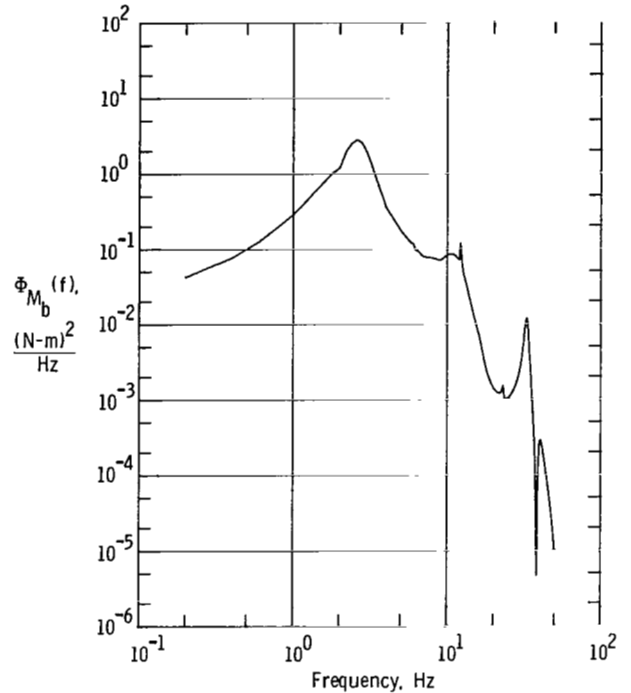
(b) Control law 1; rms = 2.253 N-m.

(c) Control law 2; rms = 4.986 N-m.

Figure 24.- Bending-moment psd at $V = 30.9$ m/sec. 48-percent semispan station.

Figure 24(b) presents a psd of bending moment for control law 1 at nominal phase and gain and at $V = 30.9$ m/sec. The character of the psd has changed compared with the system off. The peak at 3 Hz is now due not only to tunnel turbulence but to an active-control-system filter mode at almost the same frequency. (The filter-mode root loci can be seen in fig. 17.) This new mode results in a slight increase in the psd at 3 Hz compared with the system off. Another change is an increase in the frequency of the first wing bending peak (from 6.9 Hz to 10.9 Hz) and a significant reduction in its magnitude. Slight increases in the magnitude of the higher frequency modes are also predicted. The rms value of bending moment is 2.253 N-m, or a 31-percent reduction compared with the rms bending moment with the system off. This reduction is due to a decrease in the area under the psd resulting from a reduction in the response of the first wing bending mode.

Figure 24(c) presents the same data conditions for control law 2. Comparing these results with those for control law 1 (fig. 24(b)) shows that the power spectral densities are very similar for frequencies greater than 10 Hz. However, the magnitude of the psd at 3 Hz is significantly increased over that of control law 1. This is attributed to a decrease in the filter-mode damping for control law 2 compared with control law 1. (Note from figs. 17 and 20 that the flutter filter locus associated with control law 2 is closer to the imaginary axis than that for control law 1.) The resulting rms value of bending moment is 4.986 N-m, or a 54-percent increase compared with the rms bending moment with the system off. The increase in rms response is due to a much larger increase in the area under the psd around the 3-Hz peak. (Compare the decrease in area at the first wing bending peak.)

The differences in the turbulence response of the two control laws can be further explained by the data presented in figure 25. This figure presents the gain
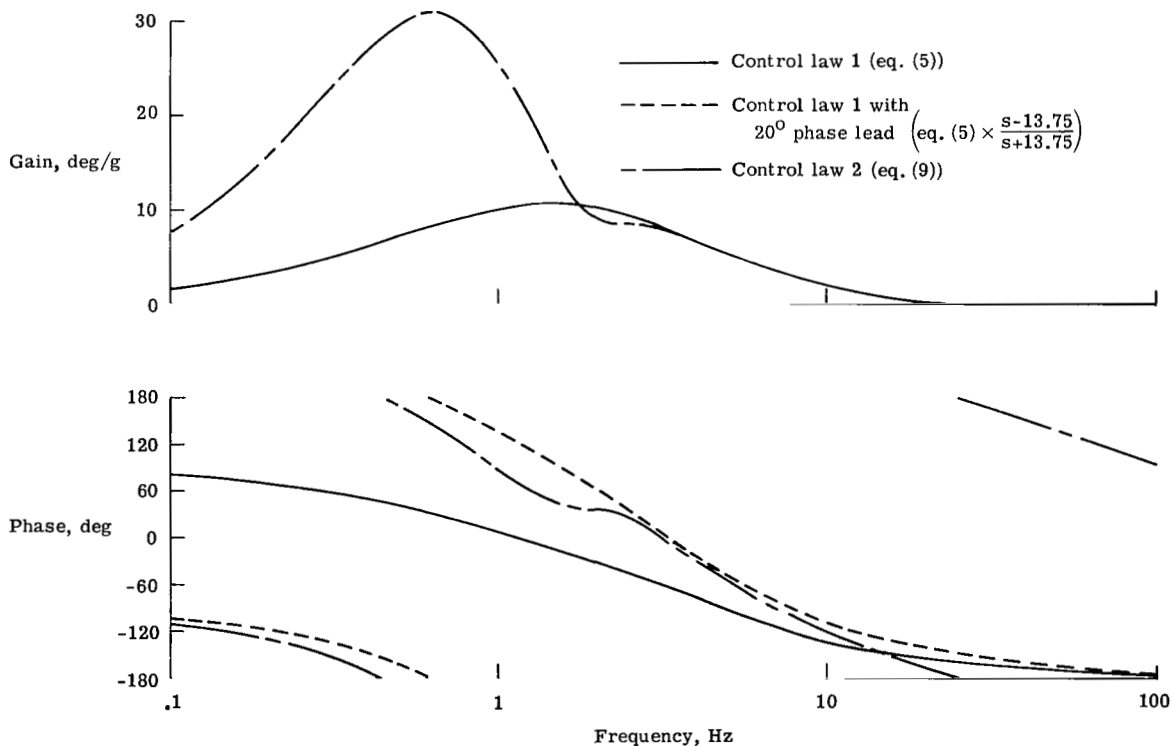

Figure 25.- Gain and phase characteristics of control laws 1 and 2.

and phase characteristics of the two control laws as a function of frequency. Included are nominal control law 1, control law 1 with 20° phase lead at 12 Hz, and nominal control law 2. Note that at 12 Hz both control laws 1 and 2 have approximately the same gain and phase characteristics. At 3 Hz the gains of both control laws are almost identical; however, the phase characteristics are significantly

(a) $\phi = -10°$; rms = 2.248 N-m.

(b) $\phi = 0°$; rms = 2.253 N-m.

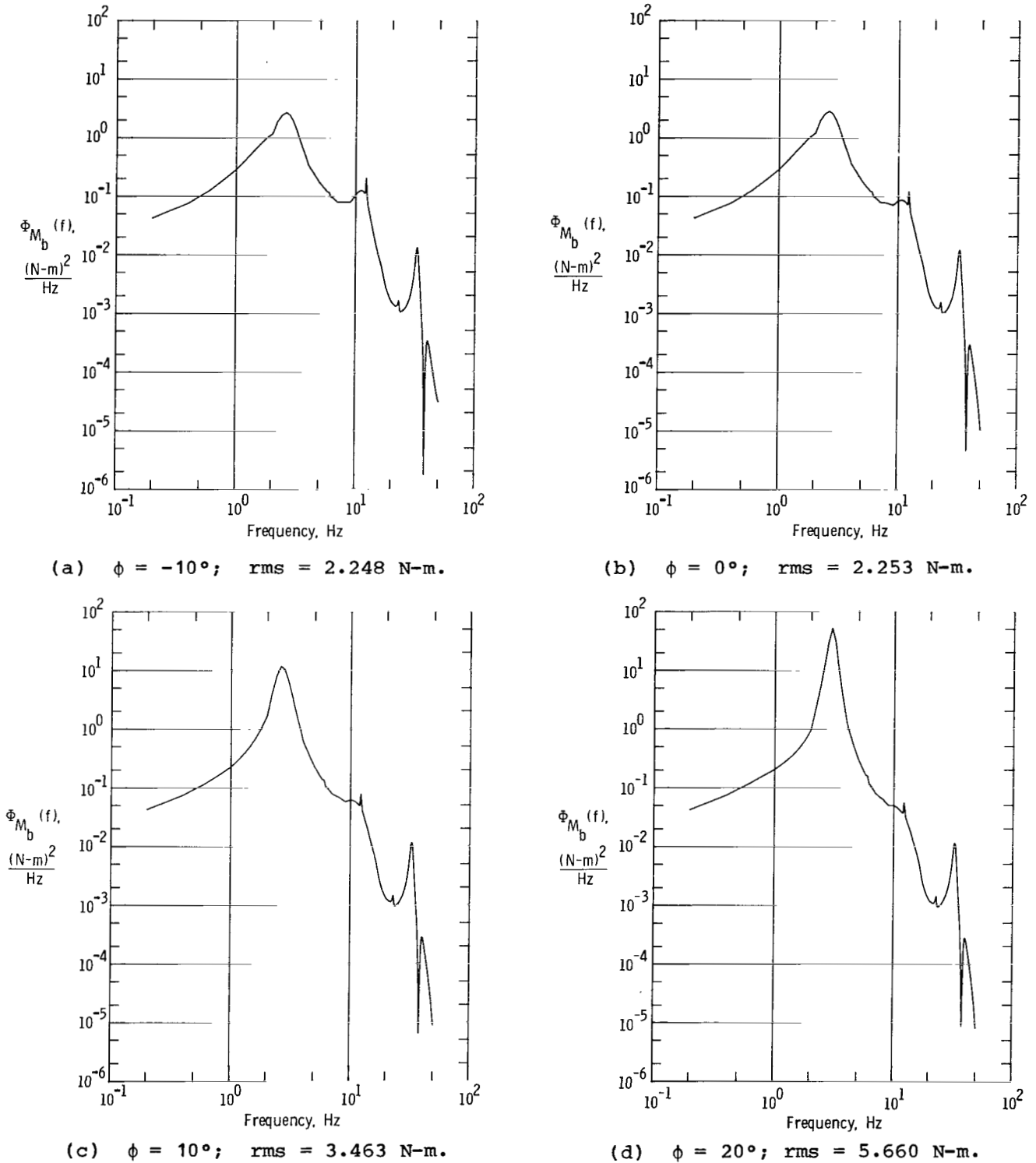(c) $\phi = 10°$; rms = 3.463 N-m.

(d) $\phi = 20°$; rms = 5.660 N-m.

Figure 26.- Bending-moment psd as function of phase angle for control law 1 at V = 30.9 m/sec. 48-percent semispan station.

different. In fact, at frequencies below the basic flutter frequency (12 Hz), the phase characteristics for control law 2 compare closely with those for control law 1 with 20° phase lead. (It can be shown that 20° of phase lead at 12 Hz introduced by the phase control filter produces a phase lead of approximately 72° at 3 Hz.) This added phase lead at low frequencies appears to be the mechanism by which the bending loads for control law 2 are increased. This is illustrated in figure 26 by presenting the power spectral densities of control law 1 as a function of phase angle. As phase lead is increased from $\phi = 0°$ to $\phi = 20°$, the rms value of bending moment increases from 2.253 N-m to 5.660 N-m, respectively. The increase in rms value of bending moment is due to significant increases in the magnitude of the 3-Hz mode. It should be noted that phase lag has very little effect on this response. The opposite is true for the primary wing flutter mode (12 Hz); that is, negative phase at the flutter frequency tends to increase response in the flutter mode (reduce stability), while positive phase tends to increase stability. These results are consistent with the stability trends presented in figure 19 for $V = 30.9$ m/sec. Comparing the results in figure 24(c) with those in figure 26(d), we see that control law 1 with 20° of phase lead behaves in a very similar manner to control law 2 in terms of bending-moment loads. It has been shown that both control laws are capable of increasing the wing flutter speed in excess of 20 percent, but with opposite effects in terms of gust loads.

## COMPARISON OF ANALYSIS AND EXPERIMENT

Flutter

Control law 1.- Control law 1 was tested during both tunnel entries. Since the majority of the data were acquired during the second entry, only a qualitative description of the results acquired during the first entry is presented. The tendency of the flutter suppression system to reduce damping in the flutter mode prior to reaching the passive wing flutter speed (see fig. 18) was visually observed during the tests. As the passive flutter speed was approached, the closed-loop damping appeared to be quite low. As the tunnel velocity was increased beyond the passive wing flutter speed, the model damping appeared to increase. A phase lead of 30° at 12 Hz was added to the control law using the phase control filter. For this phase lead the damping of the closed-loop system near the passive wing flutter speed was significantly improved. Prior to the first run, the feedback loop was closed and the model was excited with a pulsed input. Mode 8 was unstable at a frequency of approximately 42 Hz. Repeated excitation of the model at the lowest test velocity (15.4 m/sec) demonstrated that this mode becomes stable. All the results described above were predicted by analysis.

Prior to the second tunnel entry, an analysis was performed which produced the results shown in figure 18. As a result of these calculations, it was determined that phase lags introduced by modifying the actuator would result in a flutter suppression system that would have degraded performance. In fact, when the control system was tested at nominal phase and gain, the system was unstable below the passive wing flutter speed. To account for the extra phase lag introduced by the modified actuator (approximately 7° at 12.5 Hz), a phase lead of 10° was introduced into the feedback system with the phase control filter. The resulting system behaved in a manner quite similar to that observed during the first entry, except that there was some added activity in the low-frequency mode.
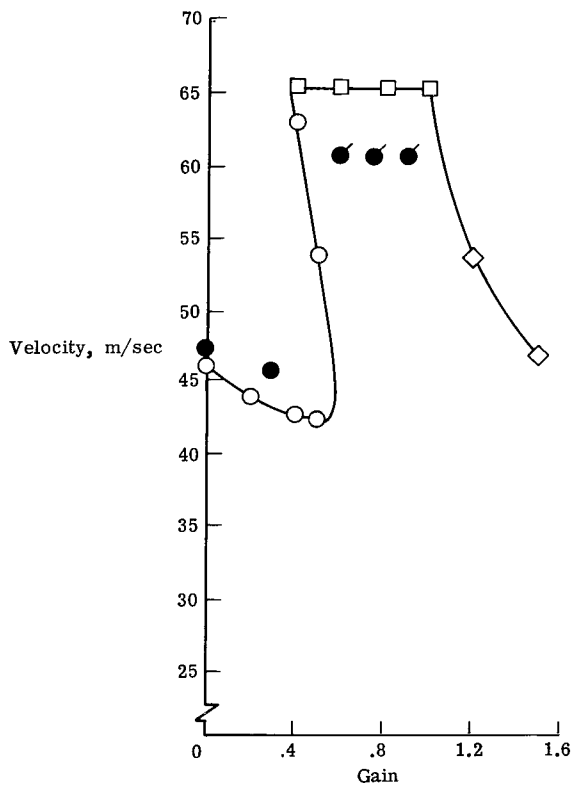
For six phase angles that were evaluated during the second tunnel entry, calculated stability boundaries are presented in figure 27 in terms of flutter velocity
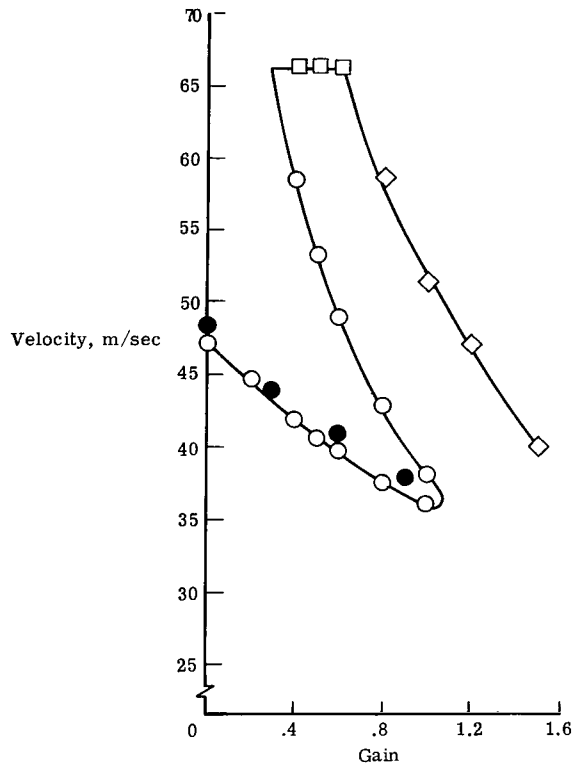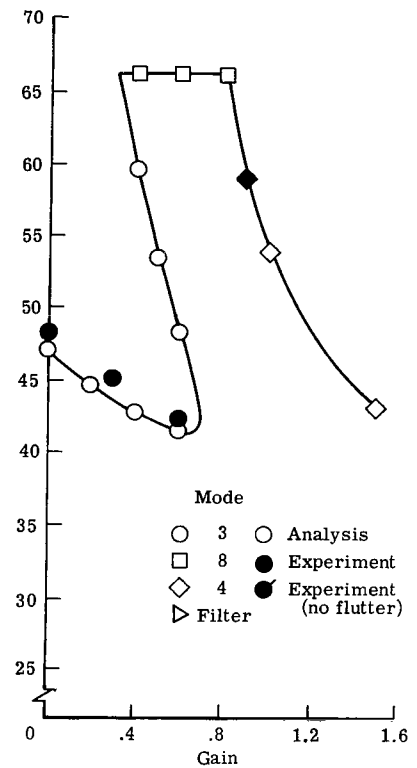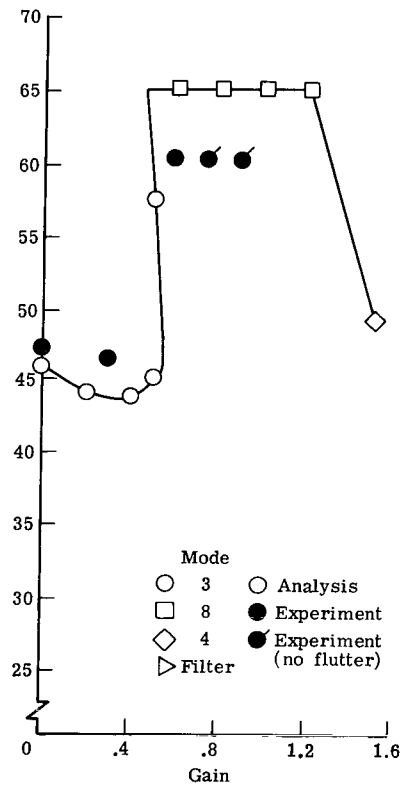
Figure 27.- Measured and predicted flutter boundaries as function of gain and phase for control law 1.
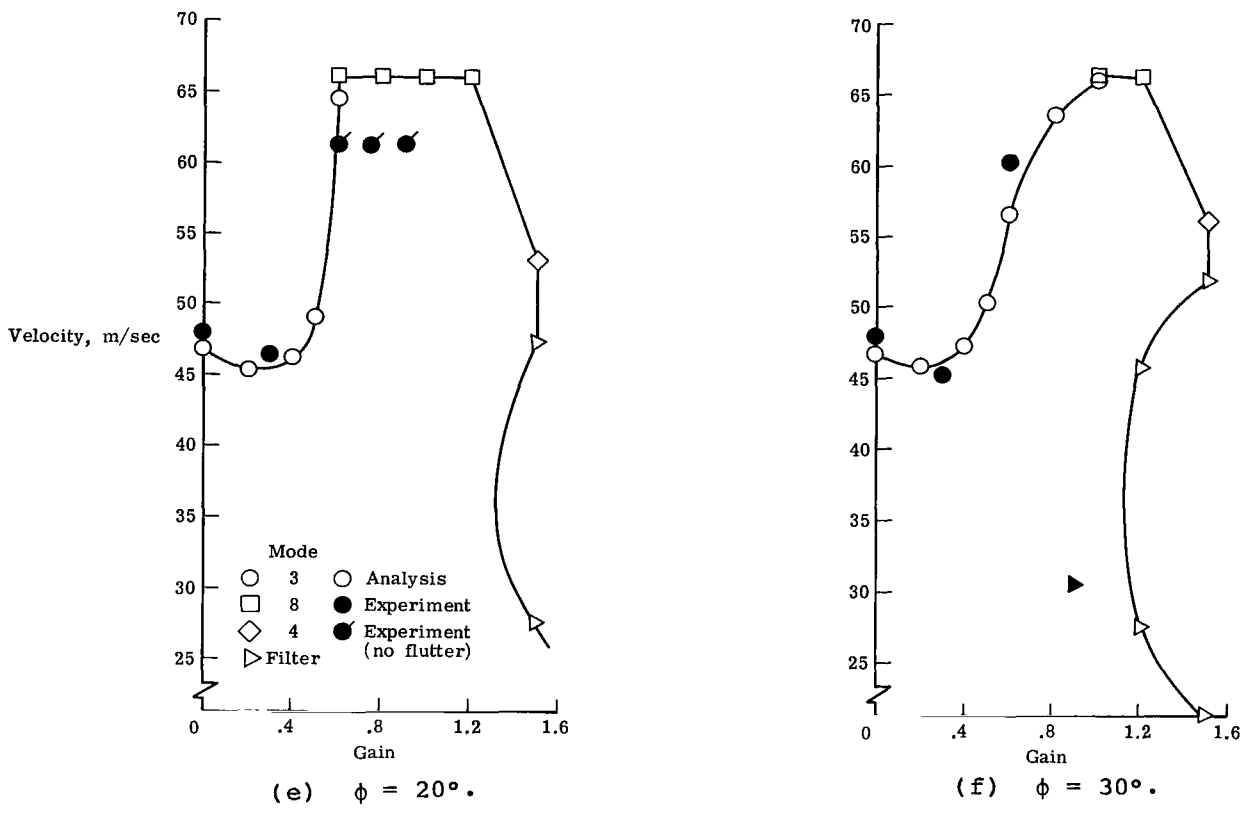
Figure 27.- Concluded.

versus system gain. Depending on phase angle, three or four distinct flutter modes are exhibited. For all phase angles analyzed, a decrease in flutter velocity is shown for mode 3 at low values of gain. At negative phase angles, the reduction in flutter velocity is more pronounced. The velocity at which mode 8 becomes unstable is nearly independent of system gain and phase. The mode 4 instability is aggravated by negative phase angles and stays relatively fixed for positive phase angles. At phase angles of 20° and above, a new flutter mode resulting from a coupling between the feedback filter mode and the first wing bending mode becomes critical. It should be noted that the phase angles in figure 27 correspond to equation (11) evaluated at $\omega = 78$ rad/sec. The phase angle produced by the phase control filter at other frequencies is significantly different.

Also presented in figure 27 are the experimentally measured stability boundaries. Two correction factors have been applied to the experimental data and will be described before comparing the results with predictions.

The first correction factor applies to system gain. It is stated in reference 2 that tests were performed in which the response of the wing to static aileron deflections was measured as a function of velocity. Typically the predicted response was 40 percent higher than measured. When a correction factor of 0.60 was applied to the control-surface aerodynamic terms, the response of the wing was predicted with greater accuracy. This correction factor was used in the gust response studies presented in reference 1 and therefore will be used in the present comparison. Since system gain is directly proportional to control-surface effectiveness, a correction factor of 0.60 was used for the experimental data before comparison with analysis (i.e., a gain setting of $K_g = 1.0$ experimentally plotted at $K_g = 0.60$).

The second correction factor deals with phase angle. Prior to most of the flutter runs during the second tunnel entry, a check of system gain and phase was performed. This was done by removing the feedback accelerometer signal from the analog computer and replacing it with a sine wave of known frequency and amplitude. This signal was used to drive the control surface through the flutter suppression electronics. Using a signal analyzer, the amplitude and phase of the control-surface motion was then compared with the input signal. At 12 Hz the predicted phase lag of the control surface with respect to the input signal is 163°. The measured phase lag varied from 170° to 176° (for an average of 173°). The experimental data will be corrected by 10° to account for this difference. (For example, for the phase control filter set to 0°, the experimental data used in the comparison will be $\phi = 10°$.)

With these two correction factors applied to the data, the experimental results compare quite well with the predictions presented in figure 27, as indicated by

1. The tendency of mode 3 to be destabilized below the passive wing flutter speed for all phase angles at low values of gain (this effect is more pronounced at negative phase angles);

2. The tendency of phase lead to stabilize mode 3 at low velocities and to have the opposite effect at higher velocities;

3. The existence of a mode 4 instability at $\phi = -10°$;

4. The existence of a coupled filter and first wing bending flutter mode at a phase lead of 30°.

From the data presented in figure 27, it is shown that increases in flutter speed in excess of 25 percent were demonstrated at phase angles of 0°, 10°, 20°, and 30°.

Figure 28 presents a comparison of measured and predicted flutter mode damping as a function of velocity for various values of phase and gain. The experimental data contain the correction factors discussed earlier. The trends predicted by analysis compare favorably with experimental trends. For example, (1) at $\phi = -20°$,
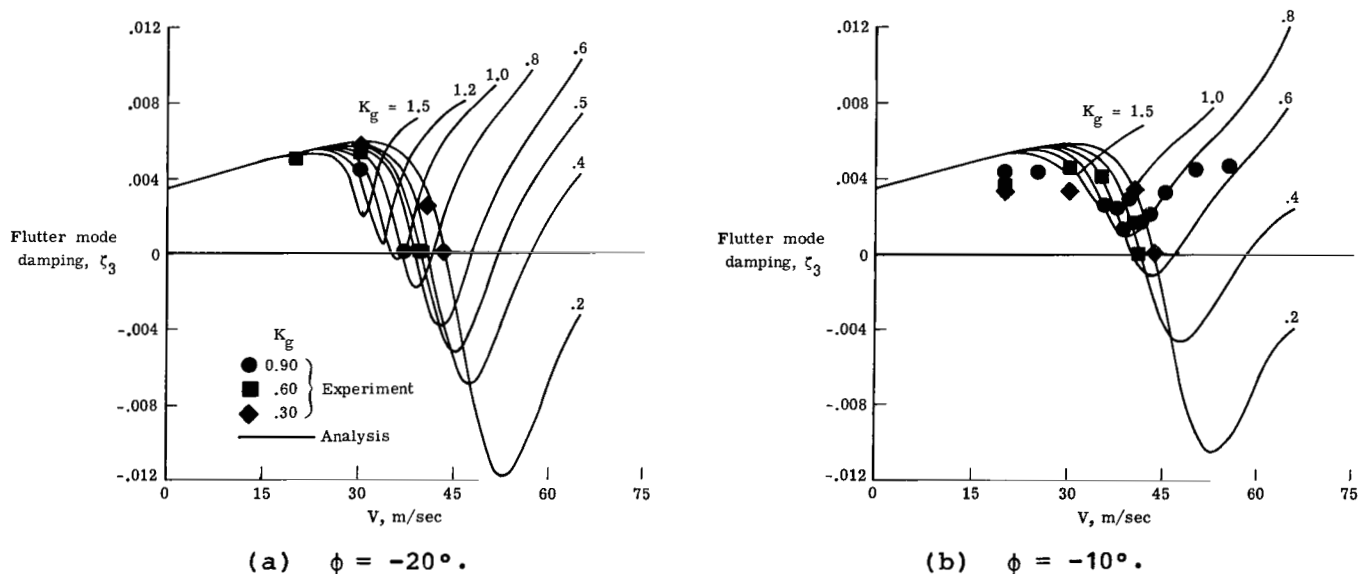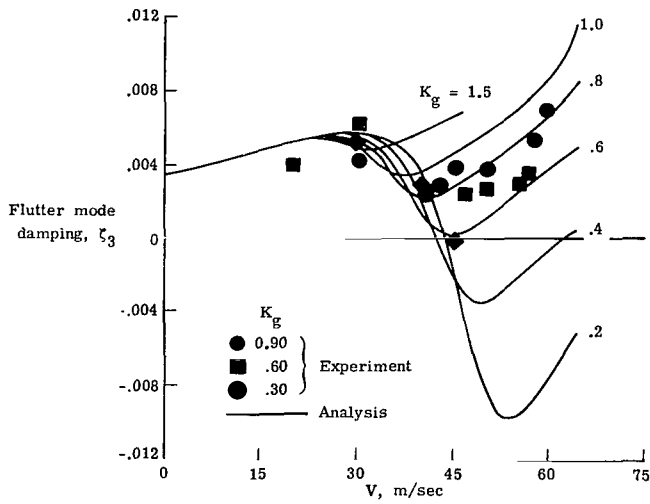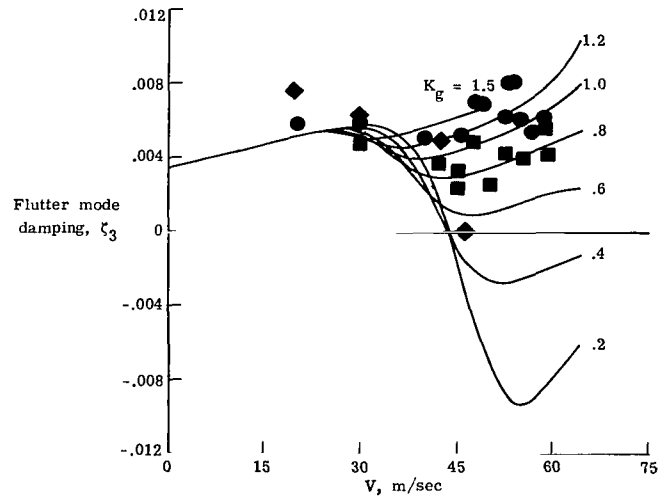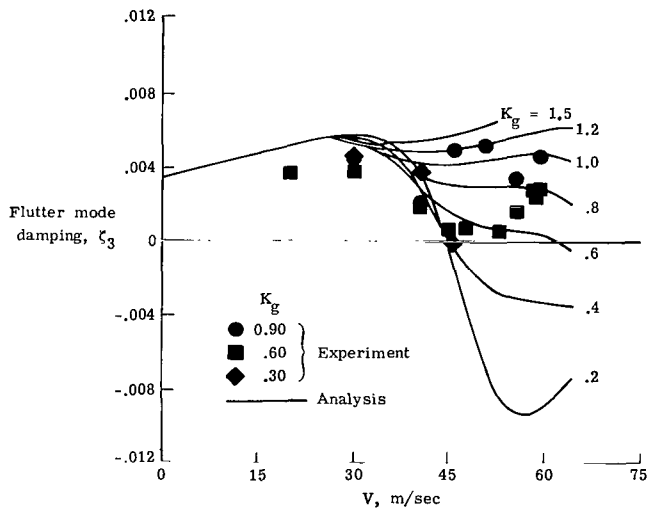

(a) $\phi = -20°$. (b) $\phi = -10°$.

Figure 28.- Flutter mode damping as function of velocity for control law 1.

(c) φ = 0°.

(d) φ = 10°.

(e) φ = 20°.
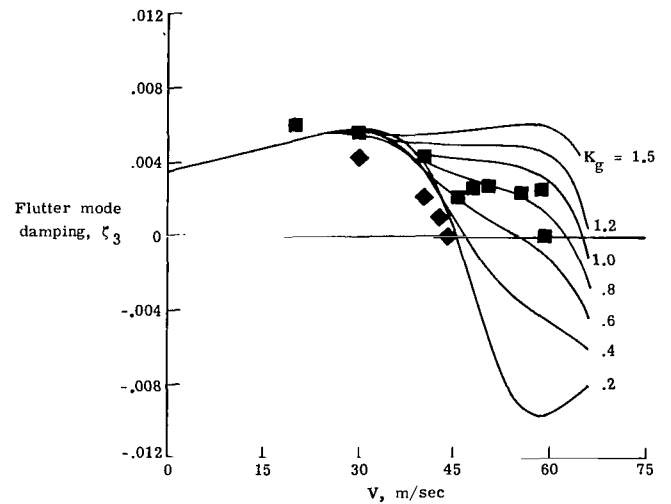
(f) φ = 30°.

Figure 28.- Concluded.

the flutter velocity decreases with increased system gain and the level of damping is reasonable; (2) at φ = -10°, the flutter velocity decreases with increasing gain until there is a level of gain which provides enough damping to preclude flutter, so that the level of damping compares favorably between analysis and experiment; (3) at φ = 0°, there is a reasonable comparison with both levels and trends; (4) at φ = 10°, somewhat higher levels of damping are measured than predicted but the trends are still predicted well - including the fact that near the open-loop flutter velocity the flutter mode damping is improved by phase lead; (5) at φ = 20°, trends and levels at the lower velocities compare reasonably well, whereas at the higher velocities some differences in level are apparent; and (6) at φ = 30°, the trends are still consistent but with generally larger differences in level. In summary, the damping trends with velocity, gain, and phase are predicted well, but with some discrepancies existing in damping level.

Control law 2.- Control law 2 was tested only during the first tunnel entry. Consequently, data are available only for gain variations at nominal phase, since control law 2 was not tested as thoroughly as control law 1.

Figure 29 presents the calculated stability boundary in terms of flutter velocity versus system gain for nominal phase ($\phi = 0°$). In general, results follow the same pattern for control law 2 as for control law 1. The model exhibited a decrease in flutter velocity for mode 3 at low values of gain. As gain is increased, the flutter velocity for mode 3 increases and the critical flutter mode becomes mode 8. The velocity at which mode 8 becomes unstable is nearly independent of system gain. Also presented in figure 29 are the experimental data measured during the test. The correction factor for the control-suface forces described earlier is also applied here. The comparison of experimental results and predictions is quite good. As indicated in figure 29, an increase in flutter speed in excess of 25 percent was also demonstrated for control law 2. No subcritical damping measurements are presented for control law 2.
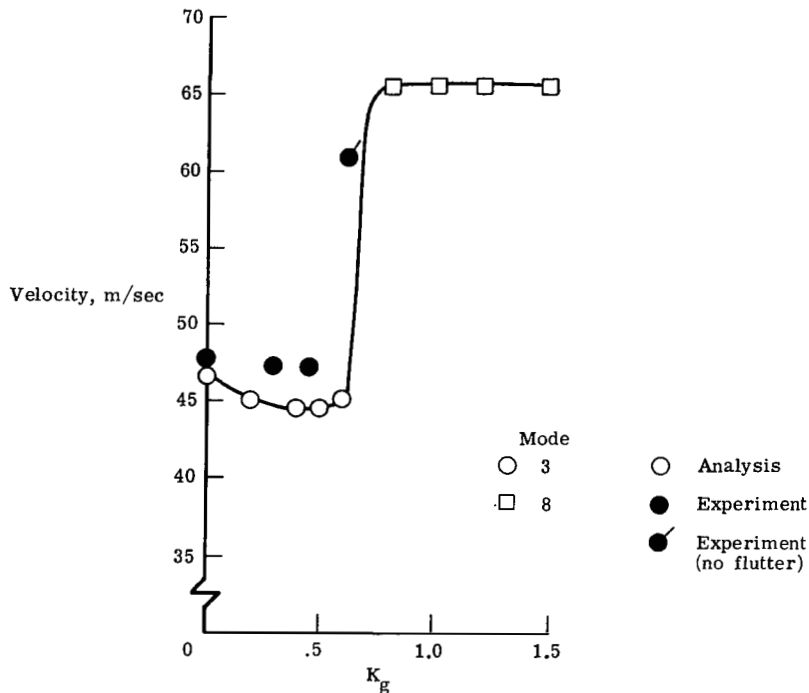
Figure 29.- Measured and predicted stability boundary as function of gain for control law 2.

Gust Response

Figure 30 presents a comparison of predicted and measured normalized values of rms bending moment, as a function of velocity, for variations in the gain and phase of control law 1. Bending moments are presented for the 48-percent semispan station and are normalized by their system-off rms values. The bending moments are plotted as a function of gain for those values of phase that were tested in the wind tunnel. A correction factor was used in system gain to account for control-surface effectiveness (i.e., at a gain setting of 1.0 the experimental data are plotted at
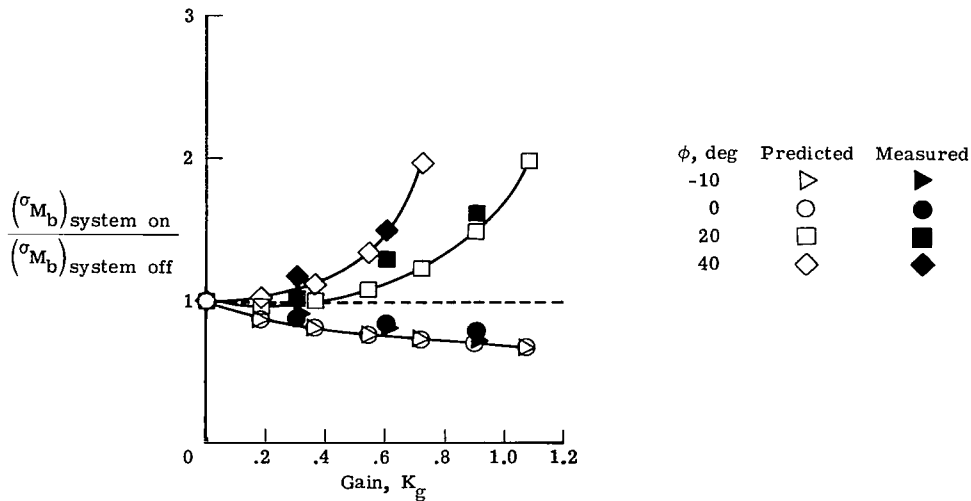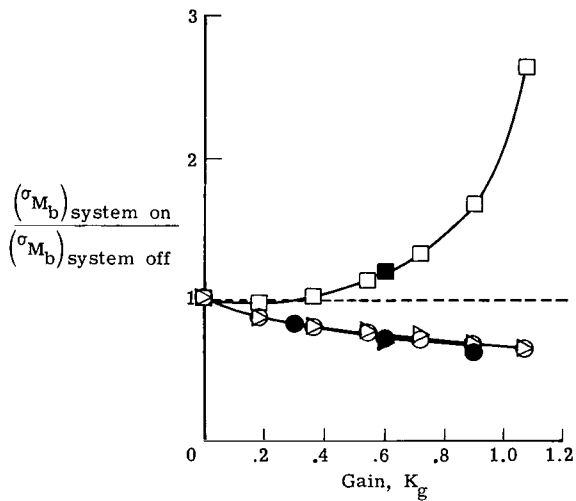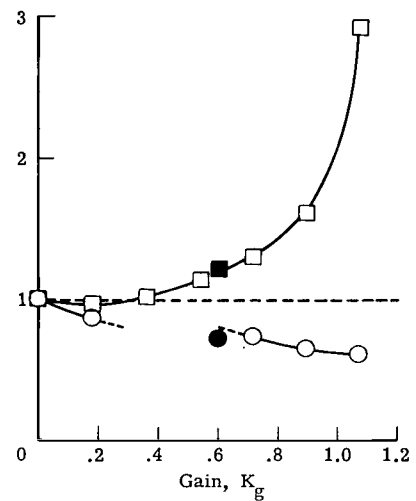
Figure 30.- Comparison of normalized bending-moment turbulence responses
for control law 1.

$K_g = 0.60$). As discussed previously, a difference was also determined between the measured and computed phase angles at the flutter frequency. This difference had a significant effect on flutter stability, but in terms of the turbulence-response results it had a minimal effect and is not included. A check of phase at the lower frequencies, where phase angle has a significant effect on the bending loads, indicated that these phase angles compare favorably with those predicted by analysis.

Figure 30(a) presents a comparison of measured and predicted data at $V = 30.9$ m/sec. At $\phi = -10°$ and $0°$ the analytical values are almost coincident. This result is verified experimentally by the closeness of the closed circle and triangle symbols at each gain. For these values of phase, the measured bending moment decreases with increased gain, up to reductions of about 20 percent at $K_g = 0.60$ and 30 percent at $K_g = 0.90$. For $\phi = 20°$ and $40°$, the normalized rms values increase with gain both analytically and experimentally. All trends predicted by analysis are verified experimentally, and the magnitude of the bending moment compares favorably with measurements.

Experimental data were also collected at tunnel speeds of 36.0 m/sec (fig. 30(b)) and 41.2 m/sec (fig. 30(c)). However, because of visibly larger wing deflections and the fear of damaging the model, turbulence-response data were collected at fewer combinations of gain and phase. Three phase angles were tested at V = 36.0 m/sec; only two phase angles were tested at V = 41.2 m/sec. The gap in figure 30(c) at zero phase is due to a predicted instability at gains of 0.36 and 0.54. (A separate analysis performed within DYLOFLEX predicts a slightly different stability boundary compared with the flutter analysis described in appendix A.) For both velocities, the trends with system gain and phase are predicted very well by analysis.

CONCLUSIONS

This paper presents the results of an experimental evaluation of two control laws that were designed to suppress flutter on a DC-10 derivative aeroelastic model. A brief description of the synthesis methodology is presented. Both control laws were tested on the model in a low-speed wind tunnel and increased the flutter speed in excess of 25 percent. Although not designed to reduce gust loads, one of the control laws was effective in reducing wing bending moments due to turbulence generated in the tunnel. The mechanism by which the control laws affected the bending loads is described. Some of the important conclusions of this study are as follows:

1. Analytically derived control laws demonstrated large increases in flutter speed. However, gain and phase margins were less than desired, and both control laws reduced the flutter mode damping at velocities below the passive wing flutter speed.

2. A comparison of analytical and measured results indicated that all flutter trends (in terms of gain, phase, and velocity) were predicted properly and that the analysis gave realistic estimates of flutter mode damping. In addition, the loads analysis accurately predicted the trends of bending-moment response to turbulence.

3. Reductions in wing bending moment on the order of 20 percent to 30 percent were predicted by analysis and verified during tunnel tests.

4. The use of correction factors to account for control-surface effectiveness and for measured actuator phase differences at the flutter frequency resulted in good correlation between measured and predicted results both for flutter and bending-moment loads as a function of control-system gain and phase.

Langley Research Center
National Aeronautics and Space Administration
Hampton, VA 23665
April 13, 1982

APPENDIX A

ANALYSIS METHODS

A description of the analysis used to calculate the stability characteristics, both with and without active controls, is given in this appendix. Also given is a description of the DYLOFLEX analysis used to calculate gust responses.

Stability Analysis

The equations of motion for a flexible vehicle can be expressed in matrix form as

$$\left([M]s^2 + [2\zeta M\omega_n]s + [K] + \frac{1}{2}\rho V^2[\hat{Q}]\right)\{q\} = -\frac{1}{2}\rho V\{\hat{Q}_G\}w_g \tag{A1}$$

where $[M]$ represents the generalized mass matrix; $[2\zeta M\omega_n]$, the structural damping matrix; $[K]$, the generalized stiffness matrix; $[\hat{Q}]$, the complex aerodynamic matrix due to motion; $\{\hat{Q}_G\}$, the complex aerodynamic vector due to gust disturbances; and $\{q\}$, the response vector. All the matrices in equation (A1) are of the size $n \times (n + r)$, where n is the number of structural modes and r is the number of active control surfaces. By expressing the response vector as

$$\{q\} = \begin{Bmatrix} q_s \\ q_c \end{Bmatrix} \tag{A2}$$

equation (A1) can be written as

$$\left([M_s \mid M_c]s^2 + [2\zeta M\omega_n \mid 0]s + [K_s \mid K_c] + \frac{1}{2}\rho V^2[\hat{Q}_s \mid \hat{Q}_c]\right)\begin{Bmatrix} q_s \\ q_c \end{Bmatrix} = -\frac{1}{2}\rho V\{\hat{Q}_G\}w_g \tag{A3}$$

where the subscript s denotes a structural quantity and subscript c, a control quantity. The equation that relates control-surface motion to wing response (control law) can be expressed as

$$\{q_c\} = [T][\phi]\{q_s\} \tag{A4}$$

where $[T]$ is the transfer function matrix and $[\phi]$ is the matrix of modal displacements at the sensor location. The transfer function matrix $[T]$ can be expressed as a rational polynomial in s by letting

$$[T] = \frac{[T_N]}{Q(s)}$$

where $Q(s)$ is a scalar polynomial representing the common denominator of all the elements of $[T]$, and $[T_N]$ is a matrix of the resulting numerators. Equation (A4) can now be expressed as

$$\{q_c\} = \frac{[T_N][\phi]}{Q(s)}\{q_s\} \tag{A5}$$

Typically, the elements of the aerodynamic matrices $\hat{Q}_s$, $\hat{Q}_c$, and $\hat{Q}_G$ are available as tabular functions of reduced frequency k, whereas the control law is expressed in terms of a rational polynomial in the Laplace variable s. The variation of the aerodynamic matrices with s can be approximated by the representation

$$[\hat{Q}] = [A_0] + [A_1]\left(\frac{b}{v}\right)s + [A_2]\left(\frac{b}{v}\right)^2 s^2 + \sum_{m=3}^{6} \frac{[A_m]s}{s + \frac{v}{b}\beta_{m-2}} \tag{A6}$$

where $[\hat{Q}]$ is $\hat{Q}_s$, $\hat{Q}_c$, and $\hat{Q}_G$ and all the matrix coefficients and β values are real. (The β values are nondimensional aerodynamic lags.) Substitution of equations (A5) and (A6) into equation (A3) and multiplication by $Q(s)$ yield a matrix polynomial expression in s of the form

$$\left([F_0] + [F_1]s + [F_2]s^2 \cdots [F_m]s^m\right)\{q_s\} = \left(\{G_0\} + \{G_1\}s + \cdots \{G_m\}s^m\right)w_g \tag{A7}$$

where the matrix coefficients $[F_j]$ and $\{G_j\}$ are functions of Mach number, velocity, and dynamic pressure. For flutter analyses, only the homogeneous part of equation (A7) is solved; that is,

$$\left([F_0] + [F_1]s + [F_2]s^2 + \cdots [F_m]s^m\right)\{q_s\} = 0 \tag{A8}$$

By using the relationship

$$\{X\} = \begin{Bmatrix} s^{m-1} & \{q_s\} \\ s^{m-2} & \{q_s\} \\ \vdots & \vdots \\ s^0 & \{q_s\} \end{Bmatrix}$$

equation (A8) can be reduced to a set of first-order equations of the form

$$s\{\overset{\cdot}{X}\} = [A]\{\overset{\cdot}{X}\} \tag{A9}$$

The eigenvalues of $[A]$ are the roots of the characteristic flutter equation. Root loci can be constructed to correspond to the variation in the eigenvalues of the system described by equation (A9) as a function of velocity.

The stability margins of the closed-loop system are determined by using a Nyquist analysis (ref. 7). To apply the Nyquist analysis, the following block diagram of the closed-loop system is used:
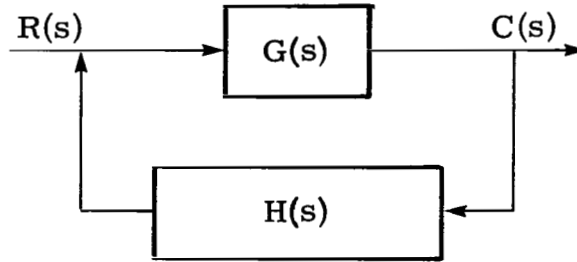
where G(s) is the transfer function of the aeroelastic model, H(s) is the control-system transfer function, and the closed-loop transfer function is defined by

$$\frac{C(s)}{R(s)} = \frac{G(s)}{1 + G(s)\ H(s)} \tag{A10}$$

In the present study, G(s) relates wing motion $\{q\}$ to control-surface motion q_c (eq. (A3) with $\{\hat{Q}_G\} = 0$ and the control-surface terms moved to the right-hand side) and H(s) relates control-surface motion to wing response (eq. (A4)). The stability margins are determined by examining a polar plot of $G(i\omega)\ H(i\omega)$ as ω varies from 0 to ∞. In a practical application ∞ is replaced by a suitable high-frequency value. A gain margin is defined as $-20\ \log_{10}$ of $G(i\omega)\ H(i\omega)$, when $G(i\omega)\ H(i\omega)$ crosses the negative real axis. A phase margin is the angle (usually expressed in degrees) between the negative real axis and the point where $G(i\omega)\ H(i\omega)$ intersects the unit circle. Gain and phase margins can have both positive and negative values.

Turbulence Response Analysis

Predicted turbulence responses for the DC-10 derivative aeroelastic model were computed using DYLOFLEX, a system of computer programs which performs dynamic loads analyses of flexible airplanes with active controls (refs. 3 and 4). The equations of motion in DYLOFLEX are formulated through a modal approach using Lagrange's equations of motion. The loads equations in DYLOFLEX are developed using the summation of forces. DYLOFLEX requires the following information to perform an analysis: mode shapes, generalized mass and stiffness matrices, lumped masses, static moments, and moments of inertia. This information pertaining to the aeroelastic model was supplied to NASA by Douglas Aircraft (ref. 2).

Equations of motion.- In the DYLOFLEX notation the equations of motion are written as

$$[M_1]\{q\} + [M_2]\{\dot{q}\} + [M_3]\{\ddot{q}\} + [M_4]\{q\} + [M_5]\{\dot{q}\} = \{c\}w_g \tag{A11}$$

where the quantities M_1, M_2, and M_3 are generalized stiffness, damping, and mass matrices, respectively; M_4 and M_5 are generalized aerodynamic matrices due to vehicle motion; C is the generalized aerodynamic column vector due to gust; q is the vector of generalized coordinates (including wing modes, aileron deflection, and active-control-system degrees of freedom); and w_g is the vertical gust velocity. Equation (A11) is solved for the generalized coordinates.

APPENDIX A

Response equation.- In this paper, wing bending moment is the response of interest. The following equation, written in DYLOFLEX notation, is the expression for wing bending moment:

$$M_b = \lfloor \bar{M}_3 \rfloor \{\ddot{q}\} + \lfloor \bar{M}_4 \rfloor \{q\} + \lfloor \bar{M}_5 \rfloor \{\dot{q}\} + \bar{C}w_g \qquad \text{(A12)}$$

This expression is seen to contain the vector of generalized coordinates and its time derivatives. Consequently, before the operations indicated in equation (A12) can be performed, $\{q\}$ and its derivatives must first be obtained from the solution of equation (A11). The quantity M_b in equation (A12) is composed of contributions from inertia forces (the term involving $\ddot{q}$), aerodynamic forces due to vehicle motion (the terms involving q and $\dot{q}$), and aerodynamic forces due to gust (the term involving w_g).

Turbulence response.- Equations (A11) and (A12) are written in the time domain. In DYLOFLEX, the equations of motion are solved and turbulence responses are computed in the frequency domain. In the frequency domain, the result of the solution of equation (A11) is a vector of frequency response functions (frf) of the generalized coordinates, $\{H_q(f)\}$. The ith element of this vector may be interpreted as the response (over all frequencies f from zero to infinity) of the ith generalized coordinate to a unit sinusoidal gust velocity (over all frequencies from zero to infinity). Vectors of frf corresponding to the first and second time derivatives of the generalized coordinates are obtained simply by multiplying the $\{H_q(f)\}$ by $i2\pi f$ and $(i2\pi f)^2$, respectively, where i is $\sqrt{-1}$. A frequency response function for wing bending moment $H_{M_b}(f)$ is obtained by making appropriate substitutions of

the frf's into equation (A12).

The quantity $H_{M_b}(f)$ is an essential ingredient in using random process theory

to compute turbulence responses. In random process theory, both the input (in this case tunnel turbulence) and the response (in this case wing bending moment) are considered to be Gaussian random processes. All the statistical information concerning these random processes (including the root-mean-square values) are contained in corresponding input and response power spectral density functions (psd). The psd's are related to each other through the frequency response function in the following simple expression:

$$\Phi_{M_b}(f) = \Phi_{w_g}(f) \left| H_{M_b}(f) \right|^2 \qquad \text{(A13)}$$

where $\Phi_{M_b}(f)$ and $\Phi_{w_g}(f)$ are the psd's of wing bending moment and tunnel turbulence, respectively, and the notation $|\;|^2$ indicates the square of the modulus of the wing bending moment frf. The quantity $H_{M_b}(f)$ is obtained in the manner out-

lined previously; $\Phi_{w_g}(f)$ is obtained from measurements of the actual turbulence in

the tunnel (and discussed in detail in appendix B). Equation (A13) is appropriate for the condition of one-dimensional (1-D) isotropic turbulence, which was not the condition in the wind tunnel. However, the assumption of 1-D isotropic turbulence was made for the purpose of the analyses performed in this paper, and this subject is also addressed in appendix B.

36

The rms value of wing bending moment is obtained by performing the following operation on the bending-moment psd:

$$\sigma_{M_b} = \left[\int_0^\infty \Phi_{M_b}(f) \, df \right]^{1/2} \tag{A14}$$

In actual practice, the upper limit of integration in equation (A14) was chosen to be 50 Hz because the turbulence psd was only defined to that frequency.

WIND-TUNNEL TURBULENCE

To perform the turbulence-response wind-tunnel tests, turbulence had to be created in the test section. The turbulence was created by installing a canvas banner across the width of the tunnel about 5 m upstream of the test section. The flapping of the banner, while the tunnel is running, creates random fluctuations in velocity. This appendix describes the nature of the wind-tunnel turbulence and examines the simplifications and approximations involved in adding an analytical representation of this turbulence to the equations of motion.

Power spectral density functions (psd's) of the vertical component of these velocity fluctuations were provided by Douglas Aircraft. A single-probe hot-wire anemometer was used to measure time histories of the vertical component of tunnel turbulence. Then, using time-series-analysis techniques on the time-history data, Douglas engineers obtained the psd's over a frequency range of 0 Hz to 50 Hz, with a frequency resolution of 0.5 Hz. At three locations in the wind tunnel (all 0.914 m downstream of the test section and 0.0762 m below the midpoint vertically; the first, 0.381 m to the left of the center line; the second, on the center line; and the third, 0.381 m to the right of the center line) psd's were obtained at tunnel speeds of 30.9, 38.6, and 44.8 m/sec.

These psd's exhibited significant dependence on both tunnel speed and location within the tunnel. This dependence can be observed conveniently by examining either the psd or root-mean-square (rms) value of the vertical component of tunnel turbulence. The rms value σ_{w_g} is defined by the equation

$$\sigma_{w_g} = \left[\int_0^{50} \Phi_{w_g}(f) \, df \right]^{1/2} \tag{B1}$$

Figure 31 illustrates the dependence of σ_{w_g} on tunnel speed. The rms value is seen to vary almost linearly with tunnel speed. The dashed line in each plot is a straight-line fit which extends from the origin through the value of σ_{w_g} at 38.6 m/sec and emphasizes how closely the variation is to a linear one.

This relationship is further illustrated by examining the variation with velocity of the value of the psd at frequency f_0. Because σ_{w_g} varies linearly with velocity and because σ_{w_g} is related to $\Phi_{w_g}(f)$ through the square root (as expressed in eq. (B1)), it is reasonable to expect that $\Phi_{w_g}(f_0)$ would vary linearly with the square of velocity (or equivalently, that $\Phi_{w_g}(f_0)$ would vary parabolically with velocity). This is, in fact, what happens, as illustrated by figure 32. The dashed curves in figure 32 are parabolas forced to pass through the origin (with zero slope) and the value of $\Phi_{w_g}(10)$ at 38.6 m/sec. The closeness

of the circle symbols to the dashed lines indicates that (at least for the range of tunnel speeds at which data were available) $\Phi_{w_g}(f_0)$ varies very nearly parabolically with tunnel speed.

(a) Left of center line.

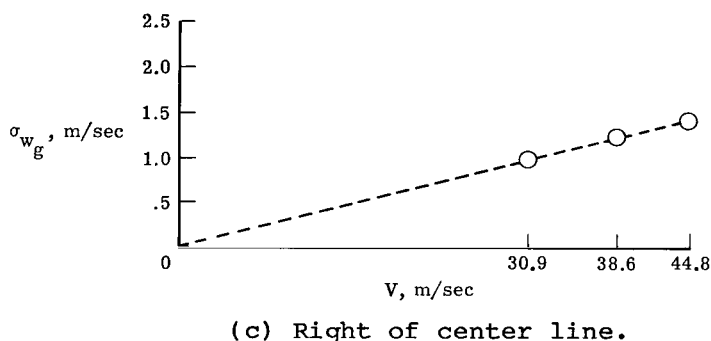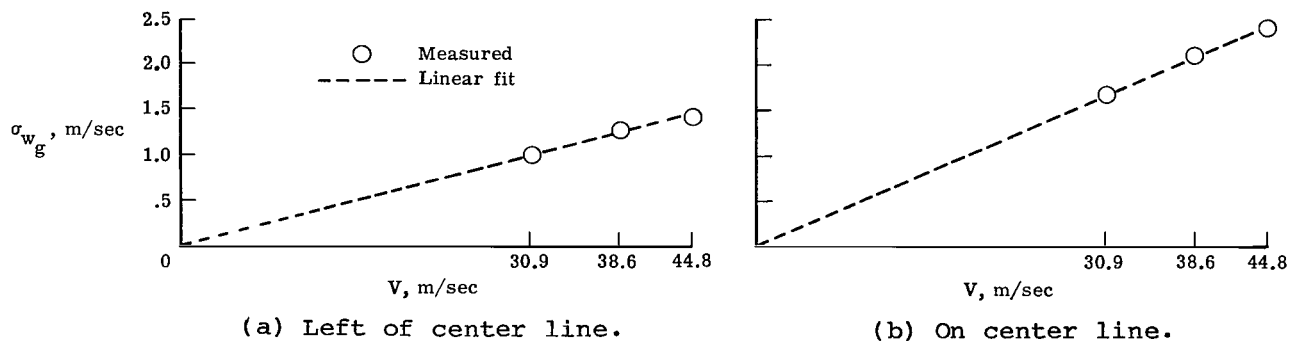(b) On center line.

(c) Right of center line.

Figure 31.- Variation with velocity of rms value of vertical component of tunnel turbulence.

(a) Left of center line.

(b) On center line.
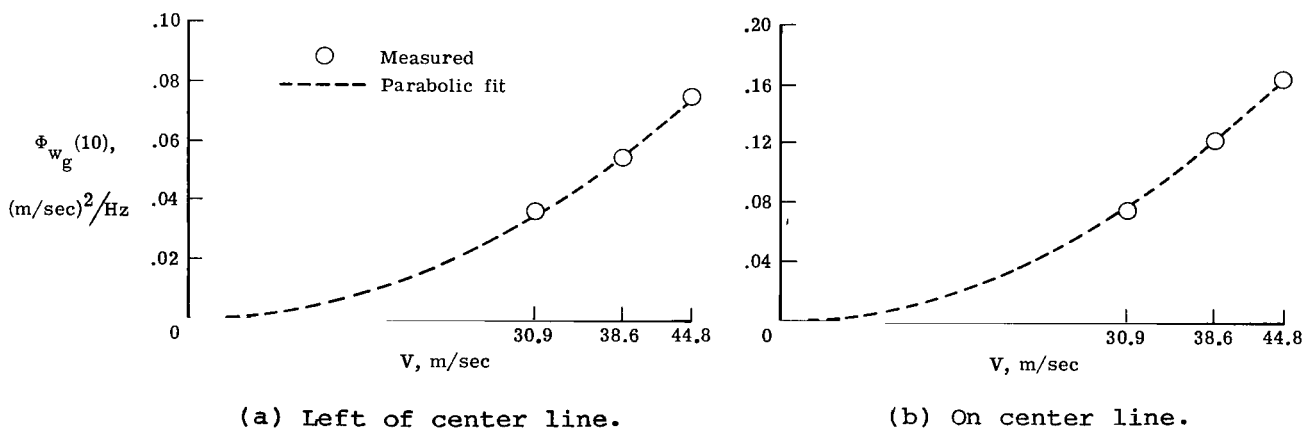
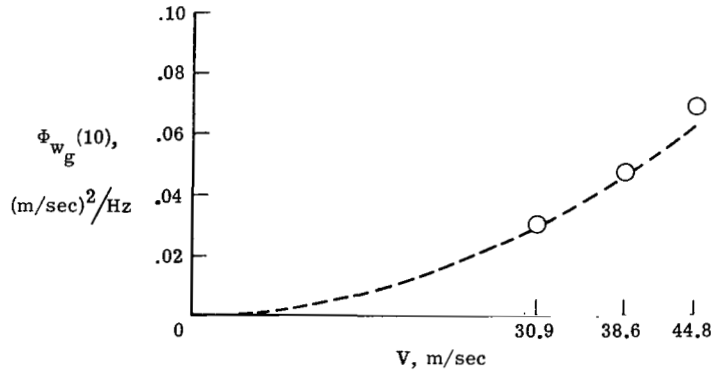Figure 32.- Variation with velocity of psd value (at 10 Hz) of vertical component of tunnel turbulence.

(c) Right of center line.

Figure 32.- Concluded.

The characteristics of the tunnel turbulence as a function of the location within the wind tunnel is shown in figure 33. Figure 33 contains plots of σ_{w_g}
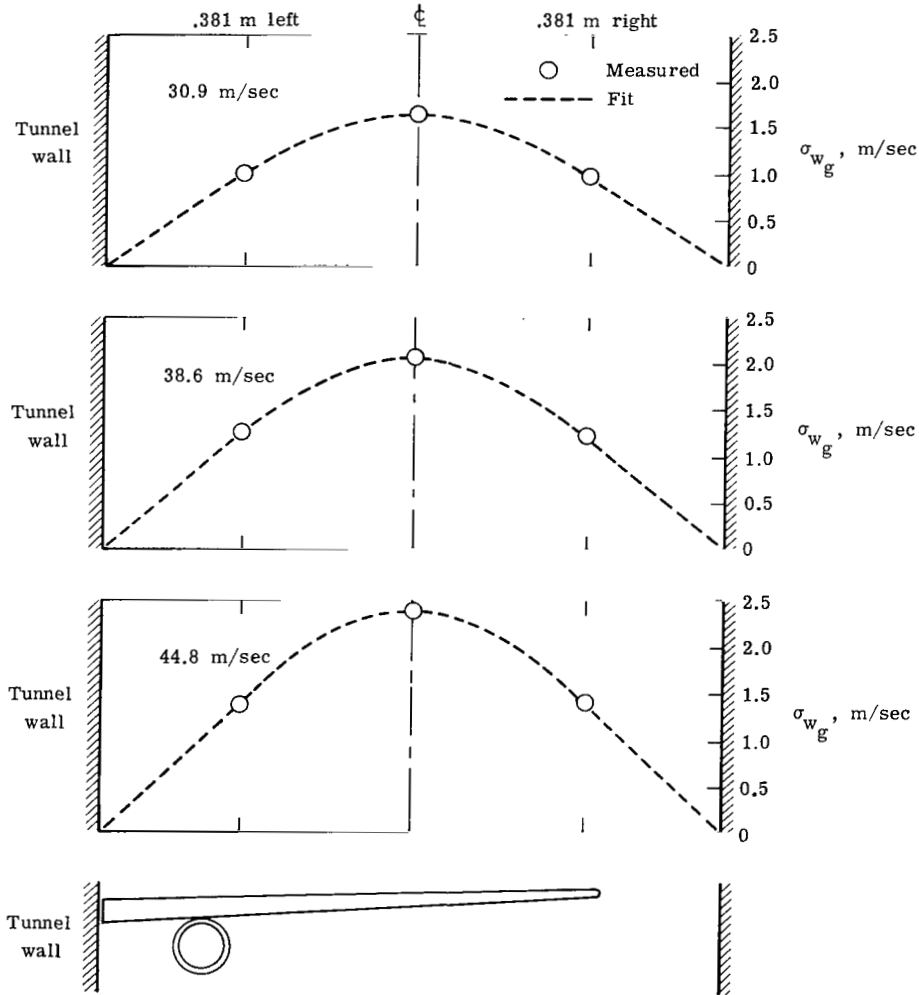

Figure 33.- Variation across tunnel width of rms value of vertical component of tunnel turbulence.

versus distance (across the wind tunnel) at each of the three tunnel speeds. The figure shows the relative positions of the wind-tunnel model, the tunnel walls, and the locations at which the turbulence was measured. These results indicate the strong two-dimensional (2-D) nature of the tunnel turbulence. The dashed-line curves in the figure are hand-drawn and are presented only to visualize possible continuous variations of σ_{w_g} across the span of the model.

Looking toward incorporating a representation of the turbulence into the equations of motion, these possible continuous variations emphasize that to properly represent the physical situations in the tunnel, a 2-D analysis is required. The following equation is the general expression (considering the turbulence to be 2-D and nonisotropic) for the psd of response quantity y (ref. 8):

$$\Phi_y = \Phi_{11}H_1\bar{H}_1 + \Phi_{22}H_2\bar{H}_2 + \Phi_{33}H_3\bar{H}_3 + \cdots$$
$$+ 2Re\left(\Phi_{12}\bar{H}_1H_2 + \Phi_{13}\bar{H}_1H_3 + \cdots + \Phi_{23}\bar{H}_2H_3 + \cdots\right) \tag{B2}$$

where

Φ_y psd of response quantity y

Φ_{ij} cross spectra of turbulence velocities at ith and jth segmented areas of the airplane

H_i frequency response function of y due to a unit sinusoidal gust velocity over ith segmental area

$\bar{H}_i$ complex conjugate of H_i

and Re denotes the real part.

To obtain the cross spectra (Φ_{ij} in eq. (B2)), simultaneous measurements of the vertical component of tunnel turbulence at each of the many points are required. In the Douglas wind tunnel, a single measurement probe was used to measure the tunnel turbulence so that, unfortunately, no simultaneous measurements of the turbulence were possible. Without such simultaneous measurements, no cross spectra could be obtained, making the full 2-D analysis, expressed by equation (B2), impossible.

A modified 2-D analysis (one with all cross spectra eliminated from equation (B2)) could still be performed and would be equivalent to making the assumption that the vertical component of turbulence in any segmented area of the model is statistically uncorrelated from that in all other (including adjacent) segmented areas. This type of modified analysis was performed by Douglas and is referred to as "spanwise uncorrelated" in reference 1. In this "spanwise uncorrelated" analysis, the various Φ_{ii} were approximated by assuming the same form (that is, same variation with frequency) of the psd's, with the value of σ_{w_g} being the only quantity which varies from segmented area to segmented area (this variation taking a form similar to the dashed-line curves in fig. 33).

For the analyses performed in this paper, the already modified form of equation (B2) was further simplified to the familiar one-dimensional (1-D) isotropic input-output relationship, expressed in a form consistent with equation (B2) as

$$\Phi_y = \Phi_{w_g} H \bar{H}$$

which can also be written as

$$\Phi_y = \Phi_{w_g} |H|^2 \tag{B3}$$

The rms value of response quantity y is obtained from the solution of

$$\sigma_y = \left[\int_0^{50} \Phi_y(f) \, df \right]^{1/2} \tag{B4}$$

Because, in this paper, the ratios of σ_y (system on) to σ_y (system off) are the quantities of interest (not the absolute levels of σ_y), it was assumed that the 1-D representation of the tunnel turbulence was adequate to predict the behavior of these ratios with control-system gain K_g and control-system phase angle ϕ.

The psd's at the tunnel center line were selected for inclusion in the 1-D analyses performed in this paper and described by equation (B3). As already mentioned, these psd's were obtained at tunnel speeds of 30.9, 38.6, and 44.8 m/sec. Yet, analyses needed to be performed at 30.9, 36.0, and 41.2 m/sec for comparison of analytically predicted rms values (σ_y) with experimentally obtained values. Estimates of the turbulence psd's at 36.0 and 41.2 m/sec were obtained by interpolating between the psd's at 30.9, 38.6, and 44.8 m/sec. This interpolation was performed by taking the values of the psd's at 30.9, 38.6, and 44.8 m/sec, one frequency at a time. At frequency f_0 the values of these psd's are, say, $\Phi_{w_g}^{30.9}(f_0)$, $\Phi_{w_g}^{38.6}(f_0)$, and $\Phi_{w_g}^{44.8}(f_0)$. Because of the nearly parabolic variation of the magnitudes of these psd's with velocity (discussed above in connection with fig. 32), a parabola was chosen (in the V-$\Phi_{w_g}^V(f_0)$ plane) which passed through the points 30.9, $\Phi_{w_g}^{30.9}(f_0)$; 38.6, $\Phi_{w_g}^{38.6}(f_0)$; and 44.8, $\Phi_{w_g}^{44.8}(f_0)$. This parabola is expressed in the form

$$\Phi_{w_g}^V(f_0) = AV^2 + BV + C \tag{B5}$$

At frequency f_0 with coefficients A, B, and C known, estimates of the values of $\Phi_{w_g}^{36.0}(f_0)$ and $\Phi_{w_g}^{41.2}(f_0)$ were obtained by substituting $V = 36.0$ and $V = 41.2$, respectively, into equation (B5). This method of estimating the turbulence psd's was repeated for about 40 frequencies between zero and 50 Hz. Figure 34 contains log-log plots of the resulting psd's. They are characterized by very pronounced peaks in the neighborhood of 3 Hz. At frequencies above 10 Hz, the psd's drop off roughly with the -5/4 power of frequency. For comparison, the corresponding slopes in the Von Kármán and Dryden psd models are -5/3 and -2, respectively.
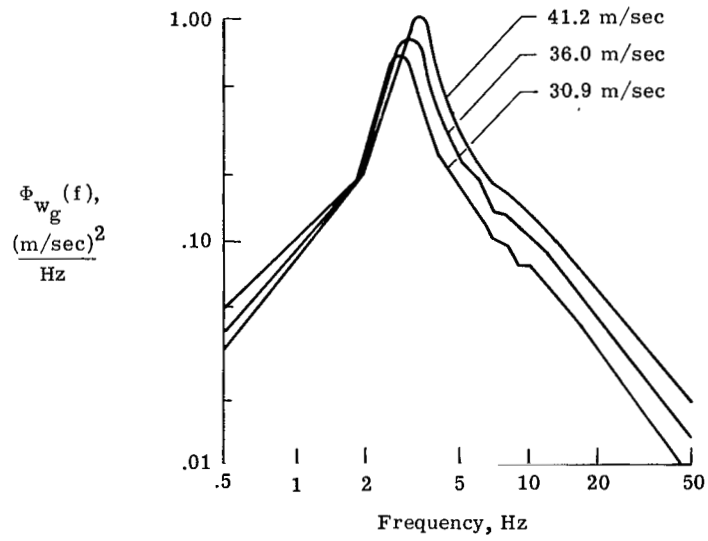
Figure 34.- Power spectral density functions of vertical component of wind-tunnel turbulence for three tunnel speeds.

REFERENCES

1. Winther, B. A.; Shirley, W. A.; and Heimbaugh, R. M.: Wind Tunnel Investigation of Active Controls Technology Applied to a DC-10 Derivative. AIAA-80-0771, May 1980.

2. Staff of Douglas Aircraft Co.: Experimental Investigation of Elastic Mode Control on a Model of a Transport Aircraft. NASA CR-3472, 1981.

3. Perry, Boyd, III; Kroll, Richard I.; Miller, Ronald D.; and Goetz, Robert C.: DYLOFLEX: A Computer Program for Flexible Aircraft Flight Dynamic Loads Analyses With Active Controls. J. Aircr., vol. 17, no. 4, Apr. 1980, pp. 275-282.

4. Miller, R. D.; Kroll, R. I.; and Clemmons, R. E.: Dynamic Loads Analysis System (DYLOFLEX) Summary. Volume I: Engineering Formulation. NASA CR-2846-1, 1979.

5. Newsom, Jerry R.; Abel, Irving; and Dunn, H. J.: Application of Two Design Methods for Active Flutter Suppression and Wind-Tunnel Test Results. NASA TP-1653, 1980.

6. Nissim, E.; and Abel, I.: Development and Application of an Optimization Procedure for Flutter Suppression Using the Aerodynamic Energy Concept. NASA TP-1137, 1978.

7. Peloubet, R. P., Jr.; Haller, R. L.; Cunningham, A. M.; Cwach, E. E.; and Watts, D.: Application of Three Aeroservoelastic Stability Analysis Techniques. AFFDL-TR-76-89, U.S. Air Force, Sept. 1976.

8. Houbolt, John C.; Steiner, Roy; and Pratt, Kermit G.: Dynamic Response of Airplanes to Atmospheric Turbulence Including Flight Data on Input and Response. NASA TR R-199, 1964.

1. Report No. NASA TP-2010	2. Government Accession No.	3. Recipient's Catalog No.
4. Title and Subtitle COMPARISON OF ANALYTICAL AND WIND-TUNNEL RESULTS FOR FLUTTER AND GUST RESPONSE OF A TRANSPORT WING WITH ACTIVE CONTROLS		5. Report Date June 1982
		6. Performing Organization Code 505-33-63-02
7. Author(s) Irving Abel, Boyd Perry III, and Jerry R. Newsom		8. Performing Organization Report No. L-15099
		10. Work Unit No.
9. Performing Organization Name and Address NASA Langley Research Center Hampton, VA 23665		11. Contract or Grant No.
		13. Type of Report and Period Covered Technical Paper
12. Sponsoring Agency Name and Address National Aeronautics and Space Administration Washington, DC 20546		14. Sponsoring Agency Code

15. Supplementary Notes

16. Abstract

Two flutter-suppression control laws have been designed and tested on a low-speed aeroelastic model of a DC-10 derivative wing. Both control laws demonstrated increases in flutter speed in excess of 25 percent above the passive wing flutter speed. In addition, one of the control laws was effective in reducing loads due to turbulence generated in the wind tunnel. The effect of variations in gain and phase on the closed-loop performance was measured and is compared with predictions. In general, both flutter and gust-response predictions agree reasonably well with experimental data.

17. Key Words (Suggested by Author(s)) Active controls Flutter suppression Gust response Aeroelasticity	18. Distribution Statement Unclassified - Unlimited Subject Category 39

19. Security Classif. (of this report) Unclassified	20. Security Classif. (of this page) Unclassified	21. No. of Pages 45	22. Price A03

National Aeronautics and
Space Administration

Washington, D.C.
20546

Official Business
Penalty for Private Use, $300

U.S.MAIL

NASA